



Steady state and lean-rich cycling study of a three-way NO_x storage catalyst: Modeling

Mengmeng Li, Sotirios A. Malamis, William Epling, Michael P. Harold*

Dept. of Chemical and Biomolecular Engineering, University of Houston, Houston, TX 77204, United States



ARTICLE INFO

Keywords:
NO_x
Three-way catalyst
Kinetics
Model
Monolith

ABSTRACT

A nonisothermal monolithic reactor model with a global kinetic formulation is developed to predict the steady-state and cyclic oxidation and reduction with CO and H₂ of a model three-way NO_x storage catalyst (TWNSC). Data were used from a parallel experimental study conducted by Malamis et al. [1] along with kinetics measurements made in the current study. The reactor model comprises a low-dimensional treatment of the transport processes and multi-site NO_x and O₂ storage combined with catalytic kinetics of the reaction steps. Kinetic sub-models of NO and CO single and co-oxidation are developed to capture the CO and NO light-off trends including inhibition effects. The sub-models are combined to simulate the catalyst performance under both steady-state and cyclic conditions. The TWNSC model predicts the steady-state product distribution spanning a range of rich conditions, along with cyclic operation features, including cycle-averaged NO_x conversion and NH₃ selectivity, and the transient species concentrations and temperature profiles over a wide range of total cycle time (TCT, 10 s–200 s) at 50% duty cycle rich. The model captures the key feature of the TWNSC using CO and H₂ as reductants. The results point to the importance of sizing the TWNSC for either NO reduction to N₂ or NH₃ formation, depending on the application. The TWNSC reactor model provides insight about reaction and transport interactions, spatio-temporal features, etc., along with guidance in the catalyst design and operation strategy optimization.

1. Introduction

Lean-burn gasoline engines have higher fuel economy and lower CO₂ emissions than spark-ignited stoichiometric engines. The three-way catalyst (TWC) is effective in concurrently converting the primary pollutants; namely, hydrocarbons (HCs), carbon monoxide (CO) and nitrogen oxides (NO_x) in stoichiometric engine exhaust. In contrast, targeted NO_x standards cannot be met with the TWC for lean burn gasoline engines due in part to the undesired consumption of NO_x reductants in the presence of excess exhaust O₂. For this reason, an alternative approach for NO_x reduction must be adopted.

Two advanced lean NO_x reduction technologies have been developed for vehicles during the past ~15 years; NO_x storage and reduction (NSR) [2,3] and selective catalytic reduction (SCR) [4]. NSR requires periodic switching between lean and rich feeds over a lean NO_x trap (LNT) catalyst containing precious group metal(s) (PGM) and alkali and alkali-earth components. During the lean operation lasting up to minutes (30–200 s) exhaust NO is oxidized to NO₂ over the PGM (Pt) and stored over barium or cerium sites in the form of nitrates and nitrites. The LNT catalyst is then exposed to a much shorter rich feed (1–20 s) to

selectively convert the stored NO_x to N₂. This is accomplished by running the engine under stoichiometric to rich fuel-air conditions which generates an exhaust containing elevated concentrations of hydrogen (H₂), CO and HC_s. The high PGM cost, byproduct (NH₃, N₂O) formation, limited sulfur resistance and hydrothermal stability, have collectively limited NSR deployment. In contrast, SCR involves the selective reduction of NO_x with NH₃ over either V₂O₅–WO₃/TiO₂ or Cu- or Fe-exchanged zeolite catalysts. The emergence of durable, active and selective Cu-SSZ-13 has led to the widespread deployment of SCR. This is in spite of the need for generating NH₃ with an onboard urea dosing system based on urea hydrolysis.

Passive SCR technology implements the SCR catalyst downstream of a TWC or LNT, the latter of which is used to generate NH₃. In so doing, the cost and footprint of the urea dosing system is avoided. Researchers at Daimler (Günther et al. [5]) and Ford Motor Company (Gandhi et al. [6]) introduced the LNT + SCR system for diesel vehicles. The synergy of LNT and SCR technology enhances the NO_x reduction efficiency, reduces undesired NH₃ emissions, and has lower PGM requirements than the standalone LNT. During the past 10 years, a group of studies has appeared that focus on the development and optimization of

* Corresponding author.

E-mail address: mharold@uh.edu (M.P. Harold).

Nomenclature	
<i>Latin symbols</i>	
C_0	Total concentration in the gas phase
$C_{p,f}$	Specific heat capacity of gas (J/kg/K)
$C_{p,w}$	Effective solid phase heat capacity (J/kg/K)
$D_{f,j}$	Diffusivity of species j in the fluid phase (m^2/s)
$D_{e,j}$	Effective diffusivity of species j in the washcoat (m^2/s)
h	Heat transfer coefficient (W/ m^2K)
$k_{me,j}$	External mass transfer coefficient (m/s)
$k_{mi,j}$	Internal mass transfer coefficient (m/s)
$k_{mo,j}$	Overall mass transfer coefficient (m/s)
k_w	Effective thermal conductivity (W/m/K)
L	Length of the monolith sample (m)
Nu_∞	Asymptotic Nusselt number
P	Transverse Peclet number
Pe_{hs}	Solid axial heat Peclet number
Pe_h	Transverse heat Peclet number
$Pe_{h,eff}$	Effective heat Peclet number
$R_{\Omega 1}$	Effective transverse diffusion length for flow area (m)
$R_{\Omega 2}$	Effective transverse diffusion length for washcoat (m)
R_i	Volumetric reaction rate (mol/ m^3 of washcoat/s)
R_g	Ideal gas constant
Sh_e	External Sherwood number
Sh_i	Internal Sherwood number
$Sh_{i,\infty}$	Asymptotic internal Sherwood number
t	Time (s)
T_f	Gas phase temperature (K)
T_s	Solid temperature (K)
ΔT_{ad}	Adiabatic temperature rise (K)
\bar{u}	Average fluid velocity in the fluid phase (m/s)
$X_{f,j}$	Cup-mixing mole fraction of species j in fluid phase
$X_{wc,j}$	Volume averaged mole fraction of species j in washcoat
z	Axial coordinate (m)
<i>Greek symbols</i>	
$\theta_{l,j}$	Stoichiometric coefficient of species j for reaction l
θ_k	Site fractional coverage of species k
ε_{wc}	Porosity of the washcoat
λ	Ratio of fluid phase diffusivity to effective washcoat diffusivity
ρ_w	Density of wall(kg/m^3)
ρ_f	Density of gas (kg/m^3)
ϕ	Thiele modulus

LNT + SCR, including evaluation of different architectures, i.e., mixed LNT + SCR sandwich [7], dual-layer [8–10], and dual brick [11–16]. The sequential LNT + SCR architecture is the most common because of its comparative simplicity. Daimler researchers [17] reported the first commercial LNT + SCR dual catalyst system outfitted on the Mercedes-Benz E-Class. A recent variant of LNT + SCR technology combines an upstream a three-way NOx storage catalyst (TWNSC) with a downstream SCR to achieve desire NOx reduction performance for lean burn gasoline vehicles. The TWNSC, which contains TWC and NOx storage components, is operated periodically to enable lean NOx reduction. This allows for periodic lean operation of the lean gasoline engine; during acceleration, the engine operates near stoichiometric while during deceleration the engine runs lean. This results in a higher overall fuel economy. The sequential TWNSC + SCR operates like the LNT + SCR; during lean operation, NOx is stored on the TWNSC while during rich operation the stored NOx is reduced and selectively generates N₂ and NH₃. The generated NH₃ is trapped by the downstream SCR catalyst. A fraction of the fed NO slips through the TWNSC unconverted during a protracted lean feed or during the initial part of regeneration (“NOx puff”). The role of the downstream SCR is to reduce the slipped NOx with NH₃ trapped on the SCR. While the TWNSC maintains similar NOx storage and reduction capability as a LNT; its application poses unique challenges. One is to constantly reduce CO and HC emissions during both lean and rich conditions while maintaining excellent NOx storage and reduction performance. Another challenge is to achieve a sufficiently high effluent NH₃ to NOx ratio (ANR) for the downstream SCR.

Several recent studies have been carried out to elucidate NH₃ formation on the TWNSC. A close-coupled TWC and SCR system studied by GM researchers [18] represents a viable aftertreatment technology for lean-burn spark-ignition direct injection (SIDI) engines. DiGiulio et al. [19] compared NH₃ formation for a TWC and a LNT of comparable PGM content and found that the passive SCR system expectedly benefits from the addition of a NOx storage component. Theis et al. [20] demonstrated that the Tier 2, Bin 2 emission standard can be achieved using a passive TWC + SCR system. Murata et al. [21] introduced a NOx trap three-way catalyst (abbreviated N-TWC), Pd/ZSM-5, to control NOx and HC emissions during cold start. The N-TWC traps NOx efficiently at low temperature (50 °C) and then reduces the stored NOx to N₂ at T > 250 °C. Adams et al. [22] studied ceria and barium effects

on NH₃ formation over a Pt/Al₂O₃ catalyst and found the addition of ceria improved the NH₃ formation by the water gas shift reaction.

During the past decade, several NSR catalyst studies have led to more accurate and efficient kinetic and reactor models [23,24]. Several different approaches have been proposed to simulate the NOx storage. Bhatia et al. and Shakya et al. [25–27] developed and applied a crystallite-scale model to describe NOx spillover from Pt to BaO along with solid-state NOx diffusion in the barium phase. The studies show that high dispersion NSR catalysts are more active and selective to N₂ while low dispersion catalysts are selective to NH₃. A dual-site NOx storage model was developed by Kromer et al. [28] as an approximate alternative which has the advantage of the crystallite-scale model. This approach is well accepted in NSR kinetic modelling to approximate the proximity of Pt and BaO and associated storage phase diffusion limitations. Koci et al. [29,30] developed a global kinetic model to capture the dynamic behavior of NH₃ and N₂ formation over a model NSR catalyst. A microkinetic formulation was incorporated into a monolithic reactor model to simulate the byproduct formation from LNT catalysts by Larson et al. [31]. Chatterjee et al. [32,33] developed a simulation tool for the LNT + SCR and demonstrated that the combined system offers improvement in NOx reduction. Ramanathan et al. [34,35] developed a TWC model and the model was modified to capture NH₃ generation and consumption trends over a TWC catalyst for a passive SCR system application. Gong et al. [36] optimized a TWC model for a TWC + SCR application, which successfully predicts N₂O formation based on the Ramanathan et al. [34,35] TWC model.

These aforementioned studies have advanced NSR modeling through the addition of TWC functionality, oxygen storage, and NOx storage and reduction with selectivity to either N₂ or NH₃. However, unlike NSR operation, an temperature rise spans the lean phase due to oxidation of reductants during TWNSC operation. This unique non-isothermal feature poses a challenge for NOx storage at high temperature during lean phase.

The objective of this combined experimental and modeling study is to develop a predictive nonisothermal TWNSC monolith reactor model applicable for steady-state and cyclic conditions. The model is developed and tuned using data from experiments spanning NOx and O₂ storage, and steady-state subsets of the overall reaction system. Various kinetic blocks are developed independently and combined to predict the overall performance of the model TWNSC using CO and H₂ as

reductants. The model-predicted spatio-temporal species concentrations, site coverages, and temperature profiles provide insight into the coupled reaction and transport processes. Finally, the model is applied to predict the impact of key operating parameters which assists in the design and optimization of the standalone TWNSC and the TWNSC positioned upstream of a SCR.

2. Experiment description

2.1. Catalyst

A model TWNSC catalyst provided by FCA US LLC was used in this study by Malamis et al. [1] to generate data for model development. The catalyst has a cell density of 600 cpsi (cell per square inch) and contains the typical components of TWC catalyst; including PGM (Pd, Pt, Rh), oxygen storage components (CeO_2 , ZrO_2), and NOx storage component (BaO). The TWNSC precious group metal mass percentage is ~ 1.2 wt.% in a Pd:Pt:Rh ratio of 73:26:1. The ICP-measured mass percentages of the oxide components is as follows: Ba = 4.7%, Ce = 10.0%, Al = 19.3%, La = 1.2%, and Zr = 8.9%. The SEM-measured washcoat thickness varied peripherally with the corner thickness about 3 times that along the wall midpoint, estimated to be 25 μm . A small catalyst sample (~ 1 cm in diameter, 1.8 cm long) was drilled from a larger catalyst piece by a dry diamond saw, then degreened in a flowing gas containing 10% H_2O , 10% CO_2 and balance Ar at 700 °C for 4 h. The catalyst was pretreated with 5% O_2 at 500 °C for 20 min. and then cooled down to a specific temperature in Ar before each experiment.

2.2. Kinetic experiments

A series of kinetic experiments were carried in a bench flow reactor system described previously by Malamis et al. [1]. The setup consists of four major units: gas supply, tubular reactor, analytical and data acquisition systems. A bank of ultra-high purity gases contained in cylinders (Praxair) and metered by mass flow controllers (MKS) were employed to simulate the exhaust gas. All experiments were carried out at a 3 L/min total flowrate (GHSV @ STP = 99,000 h^{-1}). A four-way switching valve (Valco Inc., Micro-electric two position valve) installed upstream of the reactor enabled efficient lean-rich switching in cycles as short as ~ 10 s. The effluent gas composition was monitored by a FTIR (Thermo Scientific, 6700 Nicolet) in terms of effluent species concentrations of NO, NO_2 , N_2O , NH_3 , CO, C_3H_6 , CO_2 , and H_2O .

2.2.1. NO oxidation and NOx storage

A gas mixture of 475 ppm NO, 5% O_2 , balance Ar was directed to a pre-oxidized catalyst for both NO oxidation and NOx storage measurements. The experiments were carried out at several different feed temperatures (T_f = 180–480 °C) to monitor the NO conversion and NOx storage capacity.

2.2.2. Oxygen storage

Oxygen storage capacity was investigated by CO-TPR (temperature-programmed reduction) and CO oxidation. During CO-TPR experiments, the pre-oxidized catalyst was exposed to 1000 ppm CO and balance Ar at a ramp rate of 10 °C/min spanning 50–700 °C. For the steady-state CO oxidation experiments, the catalyst was pre-oxidized and exposed to a feed of 2000 ppm CO and balance Ar over a range of temperatures (T_f = 250–500 °C).

2.2.3. CO and NO oxidation

The CO oxidation activity, CO self-inhibition, and NO inhibition were evaluated by the CO light-off experiments using 1000–5000 ppm CO, 5000 ppm O_2 and balance Ar at a ramp rate of 3 °C/min from 50 to 550 °C. NO was added at 500 ppm NO in the gas mixture.

2.2.4. Catalyst performance evaluations

Systematic experiments using steady-state or cyclic conditions were evaluated in terms of NOx reduction and NH_3 generation for the model TWNSC, as reported by Malamis et al. [1]. The catalyst was evaluated using a steady-state feed consisting of 1.6% CO, 6300 ppm H_2 , 500 ppm NO, 10% CO_2 , 7% H_2O , and a varied concentration of O_2 to achieve the prescribed stoichiometric number (S_N):

$$S_N = \frac{2C_{\text{O}_2} + C_{\text{NO}}}{C_{\text{CO}} + C_{\text{H}_2}}. \quad (1)$$

The cyclic experiments were carried out at a fixed 50% duty cycle rich (DCR = Rich Time/Total Cycle Time) and varied total cycle time (TCT). The feed gas composition of cyclic experiments consisted of 1% CO, 3300 ppm H_2 , 500 ppm NO, 10% CO_2 , 7% H_2O with varied O_2 concentrations to distinct lean and rich conditions. During the lean feed, the O_2 was maintained at 5% corresponding to $S_N = 7.4$, while during the rich feed, the O_2 was maintained at 0.3% corresponding to $S_N = 0.49$. Upon achieving a cyclic steady-state, 10 more cycles were collected and averaged to quantify the cycle-averaged NOx conversion, reductant conversion, product selectivity, and NH_3 to NOx ratio (ANR = $C_{\text{NH}_3}/C_{\text{NO}_x}$) value.

3. Model development

3.1. Reactor model

A low-dimensional model formulation of a washcoated monolith channel was used following the work of Joshi et al. [37]. The lower dimension structure is accomplished by averaging the convection-diffusion-reaction equations in the transverse direction which leads to an approximation of transverse diffusion and reaction with an overall mass transfer coefficient [37–39]. The nonisothermal low-dimensional model comprises species and energy balances in fluid and washcoat phases as well as surface species balances in washcoat phase. Key assumptions justified in previous works include: (a) laminar flow in the monolith channel; (b) negligible fluid phase axial diffusion and heat conduction in the fluid phase compared to convection; and (c) constant physical properties [39].

The species j fluid phase balance is given by:

$$\frac{\partial X_{f,j}}{\partial t} = -\bar{u} \frac{\partial X_{f,j}}{\partial z} - \frac{k_{mo,j}}{R_{\Omega_1}} (X_{f,j} - X_{wc,j}) \quad (2)$$

where the $X_{f,j}$, $X_{wc,j}$, \bar{u} , $k_{mo,j}$ and R_{Ω_1} are the gas phase and washcoat phase concentrations of species j, average fluid velocity, the overall mass transfer coefficient of species j, and the hydraulic radius, respectively. The overall mass transfer coefficient $k_{mo,j}$ is given by:

$$\frac{1}{k_{mo,j}} = \frac{1}{k_{me,j}} + \frac{1}{k_{mi,j}} \quad (3)$$

where $k_{me,j}$ and $k_{mi,j}$ are the external and internal mass transfer coefficient of species j, respectively. The external mass transfer coefficient is given by:

$$k_{me,j} = \frac{D_{f,j} Sh_e}{4R_{\Omega_1}} \quad (4)$$

where $D_{f,j}$ is the temperature-dependent gas diffusivity of species j estimated by Lennard-Jones expression [40] (Table 2). Sh_e is the position-dependent external Sherwood number using a correlation developed for fully-developed flow [41]:

$$Sh_e = Sh_{e,\infty} + \frac{0.272 \left(\frac{P}{z'} \right)}{1 + 0.083 \left(\frac{P}{z'} \right)^{2/3}} \quad (5)$$

where $Sh_{e,\infty} = 3.608$ for round square channel, $z' = z/L$ is the dimensionless length and P is the transverse mass Peclet number, where

the species j Peclet number is defined by:

$$P_j = \frac{R_{\Omega 1}^2 \bar{u}}{LD_{f,j}} \quad (6)$$

The internal mass transfer coefficient is given by:

$$k_{mi,j} = \frac{D_{s,j} Sh_i}{4R_{\Omega 2}} \quad (7)$$

where $D_{s,j}$ is the effective diffusivity ($= D_{f,j}/\lambda$) in washcoat phase and λ is assumed to be 30 based on measurements in our laboratory of alumina-based washcoats [42]. We admit that this value may be under estimated given the presence of BaO and CeO₂ in the washcoat. Sh_i is the internal Sherwood number calculated based on the expression reported by Joshi et al. [43]:

$$Sh_i = Sh_{i,\infty} + \frac{\Lambda \Phi_i^2}{1 + \Lambda \Phi_i} \quad (8)$$

where $Sh_{i,\infty} = 3.65$ and $\Lambda = 0.39$ for a rounded square channel. The Thiele modulus, Φ_i^2 is calculated by the expression [44]:

$$\Phi_i^2 = \frac{\delta^2}{D_{s,i}} \sum_j \left(-\frac{R_{i,j}(C_s)}{C_0} \right) \quad (9)$$

where C_0 is the total gas concentration ($C_0 = P_0/R_g T$).

The washcoat species balance is given by:

$$\varepsilon_{wc} R_{\Omega 2} \frac{\partial X_{wc,j}}{\partial t} = k_{mo,j} (X_{f,j} - X_{wc,j}) + \frac{R_{\Omega 2}}{C_0} \left(\sum_{l=1}^{rxn} [\theta_{lj} R_l (X_{wc,j}, T_s \theta_k)] \right) \quad (10)$$

where the ε_{wc} , $R_{\Omega 2}$, θ_{lj} , R_l , θ_k , T_s are, respectively, the porosity of washcoat, the effective thickness of washcoat, the stoichiometry of species j in reaction l, the rate of reaction l, the site fractional coverage of species k, and the washcoat temperature. The energy balance in the fluid is:

$$\frac{\partial T_f}{\partial t} = -\bar{u} \frac{\partial T_f}{\partial z} - \frac{1}{R_{\Omega 1} \rho_f C_p f} (T_f - T_s) \quad (11)$$

where ρ_f , $C_p f$, T_f , and h are the density of fluid, heat capacity of fluid, fluid temperature and heat transfer coefficient between fluid and washcoat phase, respectively. The energy balance in the washcoat is given by:

$$R_{\Omega w} \rho_w C_{pw} \frac{\partial T_s}{\partial t} = R_{\Omega w} k_w \frac{\partial^2 T_s}{\partial z^2} + h (T_f - T_s) + R_{\Omega 2} \left(\sum_{l=1}^{rxn} [R_{lj} (X_{wc,j}, T_s)] \right) (-\Delta H_l) \quad (12)$$

where $R_{\Omega w}$, ρ_w , C_{pw} , k_w , and ΔH_l are effective wall thickness, density of the wall, heat capacity of the wall, heat conductivity of the wall and enthalpy of reaction l, respectively. The surface species balance for species k is given by:

$$C_k \frac{\partial \theta_k}{\partial t} = \sum_{l=1}^{rxn} [\theta_{lk} R_{v,l} (\theta_k, X_{wc,j}, T_s)] \quad (13)$$

θ_k is the fractional coverage of surface species k [BaO_(f), BaO_(s), CeO_{2(I)}, CeO_{2(II)}, CeO_{2(III)}]. $\theta_{BaO(f)}$ and $\theta_{BaO(s)}$ represents for the fractional coverage of available fast and slow NOx storage sites:

$$\theta_{BaO(f)} = \frac{C_{BaO(f)}}{C_{BaO(f),0}} \quad (14)$$

$$\theta_{BaO(s)} = \frac{C_{BaO(s)}}{C_{BaO(s),0}} \quad (15)$$

where $C_{BaO(f),0}$ and $C_{BaO(s),0}$ represents the total fast and slow storage site concentrations while $C_{BaO(f)}$ and $C_{BaO(s)}$ represent the available fast and slow NOx storage site concentrations. $\theta_{CeO_2(I)}$, $\theta_{CeO_2(II)}$, and $\theta_{CeO_2(III)}$

represent the fractional coverage of three types of stored oxygen:

$$\theta_{CeO_2(I)} = \frac{C_{CeO_2(I)}}{C_{CeO_2(I),0}} \quad (16)$$

$$\theta_{CeO_2(II)} = \frac{C_{CeO_2(II)}}{C_{CeO_2(II),0}} \quad (17)$$

$$\theta_{CeO_2(III)} = \frac{C_{CeO_2(III)}}{C_{CeO_2(III),0}} \quad (18)$$

where $C_{CeO_2(I),0}$, $C_{CeO_2(II),0}$ and $C_{CeO_2(III),0}$ represent the three total O₂ storage site concentrations while $C_{CeO_2(I)}$, $C_{CeO_2(II)}$ and $C_{CeO_2(III)}$ represent the three O₂ covered storage site concentrations.

The initial, inlet and boundary conditions are as follows:

$$\begin{aligned} X_{f,j}(z, t=0) &= X_{f,j,0}(z) \\ X_{wc,j}(z, t=0) &= X_{wc,j,0}(z) \\ X_{f,j}(z=0, t) &= X_{j,in}(t) \end{aligned} \quad (19)$$

$$\begin{aligned} T_f(z=0, t) &= T_{fin}(t) \\ T_f(z, t=0) &= T_{f,0}(z) \\ T_s(z, t=0) &= T_{s,0}(z) \\ \frac{\partial T_s}{\partial z}(z=0, t) &= 0 \\ \frac{\partial T_s}{\partial z}(z=L, t) &= 0 \end{aligned} \quad (20)$$

$$\theta_k(z, t=0) = \theta_{k,0}(z) \quad (21)$$

Fixed parameter values used in the simulation are provided in Table 1 while temperature dependent parameters are provided in Table 2. Axial dispersion induced mixing is accounted for by a smooth curve of the lean-rich feed condition change which was recently developed by Ting et al. [45] instead of an idealized step change (An example was displayed in Fig. S-2).

3.2. Kinetic model

Building off of existing NSR and TWC kinetic models, the TWNSC kinetic model is constructed with NOx storage and TWC kinetic functionalities [34,42,46]. Tables 3 and 4 list the set of 25 reactions that are the basis for the TWNSC kinetic formulation. There have been a group of NSR models developed to date that describe NOx trapping and reduction under isothermal conditions. Shakya et al. and Bhatia et al.

Table 1
Constant parameters used in the simulation.

Parameter	Value
$R_{\Omega 1}$	225 μm
$R_{\Omega 2}$	25 μm
$R_{\Omega w}$	107.55 μm
L	0.18 m
$Sh_{e,\infty}$	4.36
$Sh_{i,\infty}$	3.65
Nu	4.36
ε_{wc}	0.4
λ	30
C_{pf}	520.3 J/kg /K
C_{pw}	1000 J/kg /K
ρ_f	1.784 kg/m ³
ρ_w	2000 kg/m ³
k_w	2 W/m/K
$C_{BaO(f)}$	25 mol/m ³ _{wc}
$C_{BaO(s)}$	70 mol/m ³ _{wc}
C_{Pt}	14.9 mol/m ³ _{wc}
$C_{CeO_2(I)}$	500 mol/m ³ _{wc}
$C_{CeO_2(II)}$	500 mol/m ³ _{wc}
$C_{CeO_2(III)}$	1024 mol/m ³ _{wc}

Table 2
Temperature dependent parameters used in the simulation.

Parameter	Value/expression
\bar{u}	$0.495 \times \frac{T}{273.15} \text{ m/s}$
$D_{f,NO}$	$1.13 \times 10^{-9} \times T^{1.7418} \text{ m}^2/\text{s}$
D_{f,NO_2}	$0.91 \times 10^{-9} \times T^{1.7184} \text{ m}^2/\text{s}$
D_{f,O_2}	$1.13 \times 10^{-9} \times T^{1.7019} \text{ m}^2/\text{s}$
D_{f,N_2}	$1.21 \times 10^{-9} \times T^{1.7019} \text{ m}^2/\text{s}$
D_{f,NH_3}	$1.62 \times 10^{-9} \times T^{1.7033} \text{ m}^2/\text{s}$
D_{f,N_2O}	$0.93 \times 10^{-9} \times T^{1.7148} \text{ m}^2/\text{s}$
D_{f,H_2}	$5.83 \times 10^{-9} \times T^{1.6725} \text{ m}^2/\text{s}$
$D_{f,CO}$	$1.13 \times 10^{-9} \times T^{1.7148} \text{ m}^2/\text{s}$
D_{f,H_2O}	$1.62 \times 10^{-9} \times T^{1.7033} \text{ m}^2/\text{s}$
D_{f,CO_2}	$0.825 \times 10^{-9} \times T^{1.7148} \text{ m}^2/\text{s}$

[42,46] developed reactor models based on global kinetic model descriptions assuming dual NOx storage sites to predict NOx storage and regeneration profiles over a NSR catalyst. Ramanathan et al. [34,35] and Gong et al. [36] developed TWC models modified to include NH₃ generation and consumption and N₂O generation over a TWC catalyst for a passive SCR system application. The global kinetic TWNSC model developed here is based on the kinetic and reactor model reported in the aforementioned studies.

3.2.1. NOx storage functionality

The NOx storage and reduction model follows from the model developed by Bhatia et al. [46] and extended by Shakya et al. [42]. The NOx storage comprises steps for NO oxidation to NO₂ (R1) on Pt sites and NO₂ storage on BaO sites [(R2) - (R4)]. The ignorance of storage by NO without oxidation and of NO/NO₂ on the ceria phase limits the strict application of the model to catalyst temperatures exceeding ~300 °C. Storage experiments described below involved the uptake of NO in a feed containing O₂ devoid of CO₂ and H₂O, justifying the consideration of BaO as the regenerated barium storage component. It is recognized in the presence of CO₂ and H₂O the regenerated barium storage component will exist as the more stable Ba(OH)₂ and BaCO₃. The dual NOx storage treatment of Bhatia et al. [38] considers fast and slow storage sites to describe the proximity of Pt and BaO and associated NOx diffusion process (steps (R2) – (R3)). Such a feature was experimentally demonstrated by Epling et al. [47] over a model NSR catalyst. The ‘fast’ sites represent the BaO sites proximal to Pt crystallites while the ‘slow’ sites represent the distal BaO sites. NOx stored on

both fast (R2) and slow (R3) storage sites are reduced by reductant H₂ in steps (R5) and (R6) forming NO, respectively, or reduced by intermediate NH₃ (formed in step R9) in steps (R7) and (R8) forming N₂. Direct barium nitrate decomposition (R4) is included to capture certain reduction features [42]. Shakya et al. [42] extended the NSR model by incorporating NH₃ generation (R9), N₂ formation (R10) and N₂O formation (R12) through reactions of reductant and gas phase NOx. Initial estimates of the parameters were adopted from Shakya et al. [42] and were further tuned based on the steady-state TWNSC experiments. Step (R11) is introduced to account for NH₃ consumption by O₂. The reaction scheme and rate expressions are reported in Table 3.

3.2.2. TWC functionality

The reactions that account for catalysis associated with NO reduction, H₂ and CO oxidation, and ceria oxidation and reduction are shown in Table 4, steps (R13) – (R25). Steps (R13) – (R25) are adopted from the TWC kinetic model developed by Ramanathan et al. [34]. The oxygen storage capacity of the TWNSC was calibrated by CO-TPR and CO oxidation experiments in order to predict the transient oxidation trends during cyclic operation. Three types of oxygen storage sites (Site I, II, and III) are identified and the corresponding model developed to predict the CO oxidation reactions with stored oxygen. The CO oxidation (R14) kinetics were estimated by a series of CO TPO experiments and corresponding modification is made to account for the elimination of CO self-inhibition by additional ceria, along with the NO inhibition effect.

Several sub-models are combined to capture the transient profiles of the TWNSC kinetic model through a step-wise approach. Fig. 1 is a block diagram schematic of the TWNSC model development approach. The solid boxes represent the kinetic models developed in this study, while the dashed boxes represent models adopted from the previous literature [34,35,42,46]. Kinetic parameters listed above the solid lines represent those extracted from previous sub-models and used in the subsequent model. For example, the A_{N-1} and E_{N-1} parameters from the NO oxidation sub-model are utilized in the NOx storage sub-model. The bold-blue parameters are those that are re-tuned in the next model. Dashed lines indicate particular chemistries used as-is. The detailed model development procedures are described below. A table provided below lists the TWNSC reactions and corresponding reactions developed in the sub-models.

The NO oxidation experiments were carried out over a wide temperature range to estimate the kinetic parameters based on the microkinetic model assuming O₂ adsorption as the rate-determining step, developed by Bhatia et al. [46]. CO inhibition of NO oxidation was

Table 3
Reaction scheme and rate expression used for NOx storage functionality.

#	Reactions	Rate Expression
R1	NO Oxidation	$NO + \frac{1}{2}O_2 \leftrightarrow NO_2$
R2	NOx Storage	$k_2 X_{wc,NO_2} X_{wc,O_2} \theta(f)^2 C_{BaO}(f)$
R3	Reactions	$k_3 X_{wc,NO_2} \theta(s)^2 C_{BaO}(s), 0$
R4		$k_4 (1-\theta(f))^2 C_{BaO}(f), 0$
R5	Stored NOx Reduction	$k_5 X_{wc,H_2} (1-\theta(f))^2 C_{BaO}(f), 0$
R6		$k_6 X_{wc,H_2} (1-\theta(s))^2 C_{BaO}(s), 0$
R7		$k_7 X_{wc,HN_3} (1-\theta(f))^2 C_{BaO}(f), 0$
R8		$k_8 X_{wc,HN_3} (1-\theta(s))^2 C_{BaO}(s), 0$
R9	NH ₃ formation & consumption	$k_9 X_{wc,NO} X_{wc,H_2} C_{PGM}$
R10		$k_{10} X_{wc,NO} X_{wc,NH_3} C_{PGM}$
R11		$k_{11} X_{wc,NH_3} X_{wc,O_2} C_{PGM}$
R12	N ₂ O Formation	$k_{12} X_{wc,NO} X_{wc,H_2} C_{PGM}$

$$\text{Expression of } Ki: K_1 = 5.91 \times 10^{-7} \exp(1.29 \times \frac{10^4}{T}); \quad K_2 = 8.1 \times 10^{-9} \exp(9.62 \times \frac{10^3}{T}); \quad K_3 = 1.8 \times 10^0 \exp(-6.78 \times \frac{10^3}{T}); \quad K_4 = 1.4 \times 10^{-8} \exp(1.18 \times \frac{10^4}{T}); \\ K_5 = 4.94 \times 10^{-4} \exp(1.56 \times \frac{10^4}{T}).$$

Table 4

Reaction scheme and rate expression used for TWC functionality.

#	Reactions	Rate Expression
R13	Oxidation Reactions	$2H_2 + O_2 \rightarrow 2H_2O$
R14		$2CO + O_2 \rightarrow 2CO_2$
R15	Gas Phase NOx Reduction	$2H_2 + 2NO \rightarrow 2H_2O + N_2$
R16		$2CO + 2NO \rightarrow 2CO_2 + N_2$
R17	Water Gas Shift	$CO + H_2O \leftrightarrow CO_2 + H_2$
R18	Ceria Oxidation & Reduction	$O_2 + 2Ce_2O_3(I) \rightarrow 4CeO_2(I)$
R19		$2NO + 2Ce_2O_3(I) \rightarrow 4CeO_2(I) + N_2$
R20		$H_2 + 2CeO_2(I) \rightarrow Ce_2O_3(I) + H_2O$
R21		$CO + 2CeO_2(I) \rightarrow Ce_2O_3(I) + CO_2$
R22		$O_2 + 2Ce_2O_3(II) \rightarrow 4CeO_2(II)$
R23		$2NO + 2Ce_2O_3(II) \rightarrow 4CeO_2(II) + N_2$
R24		$H_2 + 2CeO_2(II) \rightarrow Ce_2O_3(II) + H_2O$
R25		$CO + 2CeO_2(II) \rightarrow Ce_2O_3(II) + CO_2$

Expression of G (Inhibition Term): $H = (1 + K_{CO}X_{wc,CO})^2(1 + K_{NO}X_{wc,NO})$, where $K_{CO} = 4.314\exp(\frac{485}{T_s})$. $K_{NO} = 8.699 \times 10^5\exp(\frac{-3685}{T_s})$.

ignored on the basis that CO is consumed at a lower temperature than NO light-off occurs. The dual NOx storage model developed by Shakya et al. [42] was applied to estimate kinetic parameters and associated fast and slow storage sites loadings based on the NOx uptake experiments. Since ceria plays an important role in the TWNSC, the CO-TPR and CO oxidation reaction with stored O₂ were carried out to calibrate the O₂ storage capacity (OSC) and estimate associated kinetic parameters. The kinetic parameters of the parallel CO oxidation were estimated by a series of CO TPO experiments and further modified by incorporating the oxygen storage and reduction model. To account for mutual inhibition effects during CO and NO oxidation over the TWNSC, a CO + NO co-oxidation model was developed based on the individual CO oxidation and NO oxidation models developed in this work and the reactions of NO reduction by CO forming N₂O and N₂ from Ramanathan et al. [34]. To capture NO inhibition of CO oxidation, a NO inhibition term was added to modify the CO oxidation rate expression, and the kinetic parameters of NO oxidation reaction were tuned to account for the impact of CO on NO oxidation. The kinetic parameters for N₂O formation were estimated based on the co-oxidation experiments.

The cyclic TWNSC model followed the same reaction scheme and rate expression developed for the steady-state model with most of the common kinetic parameters used without further tuning. Some additional parameter tuning was needed to capture certain transient trends during cyclic operation for total cycle time (TCT) of 50 s, including pre-exponential factors for NOx storage, stored NOx reduction over fast storage sites, NH₃ formation and consumption, and CO oxidation. The literature parameter values as mentioned above (pre-exponential factors and activation energies of Steps [(R1)-(R25)]) [34,35,42,46] were used as the initial guess and followed by tuning to get a reasonable fitting for each sub-model. A Levenberg-Marquardt scheme assisted in the convergence to final parameter estimates. Additional details are provided in Section 4.

4. Results and discussion

4.1. NO oxidation and NOx storage kinetics

The addition of the NOx storage function on BaO enables NOx

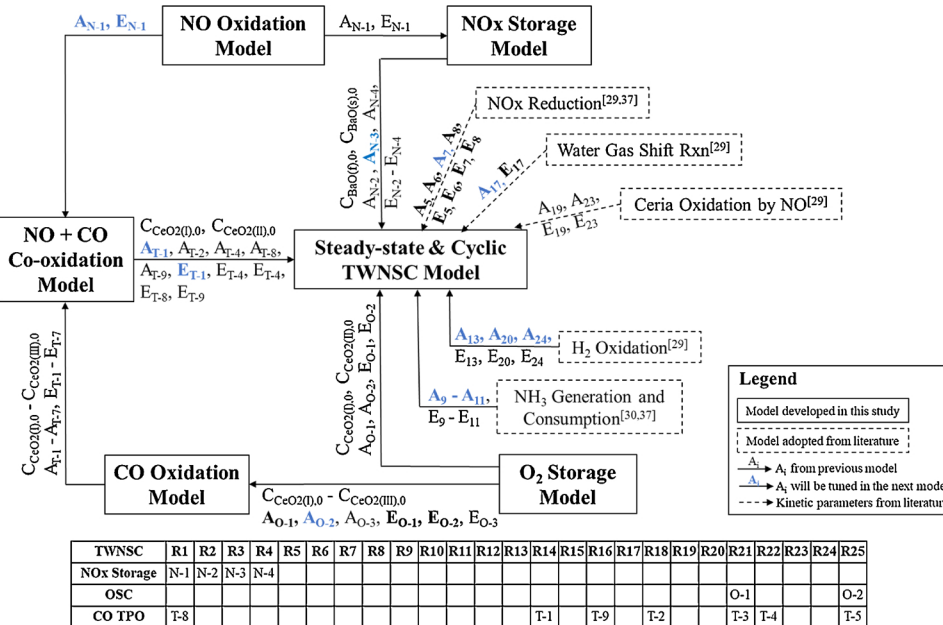


Fig. 1. Schematic of Model Development Approach.

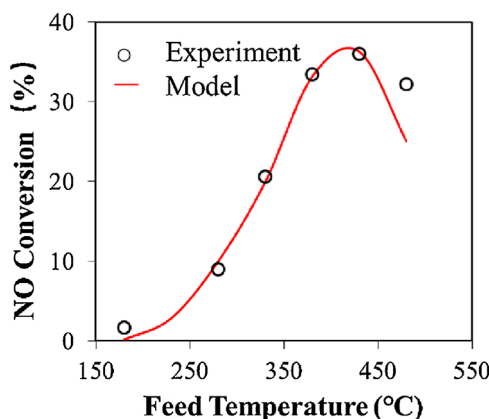


Fig. 2. Comparison of experimental and model-predicted steady-state NO conversion as a function of catalyst temperature. [Condition: NO = 475 ppm, O₂ = 5% and balance Ar.].

trapping and reduction on the TWNSC. An experimental series was carried out to evaluate and quantify the NO oxidation kinetics and NOx storage capacity and kinetics. Fig. 2 shows the dependence of NO conversion on feed temperature while Fig. 3 shows the NOx uptake profile at T_f = 330 and 380 °C. The TWNSC exhibits NO oxidation features similar to those reported elsewhere; e.g. the NO oxidation conversion achieves a maximum at intermediate temperature, consistent with NO oxidation over a Pt/BaO/Al₂O₃ catalyst [46]. The conversion increases with temperature to the left of the maximum, limited primarily by the kinetics, while the conversion decreases with temperature to the right of the maximum due to reaction equilibrium limitations. The maximum conversion (38%) is lower than the ~60% reported by Bhatia et al. [41], likely due to the lower Pt loading in the current work compared to the 3.7 wt.% used in [41], as well as the presence of BaO which is known to reduce the NO oxidation activity of Pt [41]. The solid line shown in Fig. 2 is the model-predicted NO conversion, which predicts the conversion in the kinetic regime and the maximum NO conversion at T_f = 380 °C. The pre-exponential factor and activation energy values provided by Bhatia et al. [46] were adjusted to get the fit shown in Fig. 2. The pre-exponential factor was reduced by a factor of 8 while the activation energy decreased to 28 kJ/mol. The model-predicted NO conversion agrees with the measurements with some deviation at temperatures to the right of the maximum. It is anticipated that the conversion would approach the equilibrium value at even higher temperatures, consistent with Watling et al. [48]. The higher temperatures were not studied to minimize catalyst deactivation.

Fig. 3 compares the measured and predicted transient effluent NOx (NO and NO₂) concentrations profiles at 330 and 380 °C. The NOx storage site loadings were adjusted; i.e. fast storage site loading from 75 to 25 mol/m³ wc and slow storage site loading from 250 to 70 mol/m³ wc. These adjustments follow from the TWNSC containing less BaO (~10 wt.% BaO) than the typical NSR catalyst (~20–30 wt.%) [49]. The storage parameters reported in Table 3[(R1) – (R4)] were estimated using the transient NO and NO₂ effluent concentrations at T_f = 330 °C. The pre-exponential factors of R2 - R4 The kinetic parameters are provided in Table S-1 of the Supplementary Material. These were adjusted from the values reported by Shakya et al. [42] in order to capture the NOx effluent profile within 500 s at a specified temperature. The data and model predictions reveal the heterogeneity of the NOx uptake in terms of faster and slower sites. The breakthrough followed by the more gradual approach to the NO feed concentration value indicate initially rapid then slower uptake on fast and slow sites, respectively. The NO₂ breakthrough at 65 s indicates the catalyst is able to store NO₂ up to 65 s while the breakthrough of NO suggests the limitation of NOx storage is mainly due to the slow NO oxidation reaction.

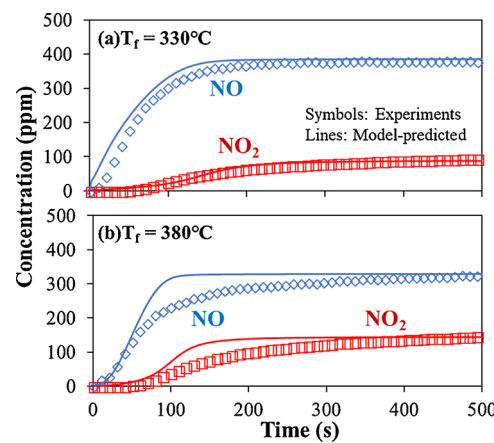


Fig. 3. Comparison of experimental and model-predicted effluent NOx concentration profile during storage at (a) 330 °C, (b) 380 °C. Symbols: experiments; Lines: model-predicted [Condition: NO = 475 ppm, O₂ = 5% and balance Ar.].

4.2. Oxygen storage kinetics

In the conventional TWC, there is a narrow window of air to fuel ratio to simultaneously achieve a high conversion of CO, hydrocarbons (by oxidation) and NO (by reduction). To widen this operational window, particularly under transient conditions, oxygen storage components, i.e. ceria and zirconia, are added to serve as an oxygen source/sink. Previous studies have modeled the contribution of oxygen storage capacity on the TWC performance [44,50,51]. Quantitatively capturing the OSC features of the TWNSC is essential to predict the overall performance.

A set of experiments was conducted using CO as a probe molecule to measure the OSC of the TWNSC. CO temperature-programmed reduction (TPR) was carried out in which the pre-oxidized TWNSC catalyst was exposed to 1000 ppm CO in balance Ar at a ramp rate 10 °C/min. In addition, CO oxidation (constant temperature) experiments were conducted in which 2000 ppm CO balance Ar at specific feed temperature (250, 300, 400, 500 °C) for 1 h, respectively. Fig. 4a shows the transient CO₂ effluent concentration and CO consumption concentration during the CO-TPR experiments. Three relative maxima in CO₂ yield were observed at 165, 285 and 630 °C indicating that CO reacts with three types of stored oxygen. These are interpreted as follows. Once the ramping temperature reaches 165 °C, CO reacts with adsorbed atomic oxygen (Site I) located at the interface of PGM-CeO₂ [52]. Upon reaction, the formation of CO₂ at Site I leaves an oxygen vacancy, creating a concentration gradient between Site I and distal ceria (Site II). As the temperature increases, the increasing rate of CO₂ formation suggests the consumption of oxygen supplied by distal ceria. When the temperature increases beyond 500 °C, the CO oxidation by oxygen directly adsorbed on ceria (Site III) occurs without any involvement of PGM. These observations are consistent with the results of Serre et al. [52].

CO concentration as a function of exposure time is shown in Fig. 4b. The inset figure shows CO concentration during the first 100 s of exposure. Three distinguishable sites are observed: Site I, 0–25 s; Site II, 25–150 s; Site III, 150 – 1000 s. During the first 25 s, all CO is consumed by the easily reducible oxygen adsorbed on Site I. Then CO gradually breaks through, indicating slower oxidation with the distal oxygen atom adsorbed over Site II. Finally, ~100 ppm CO slowly reacts with oxygen stored by the bulk ceria (Site III). The loadings of the first two storage site types (Site I + II) were estimated by the oxidation of CO with the stored oxygen at 400 °C (Fig. 4b). The Site I loading was estimated based on the initial consumption of CO within 25 s after exposing to the pre-oxidized TWNSC. The Site II loading was estimated based on the consumption of CO from 25 to 150 s. Finally, Site III was determined by the difference between total ceria site concentration

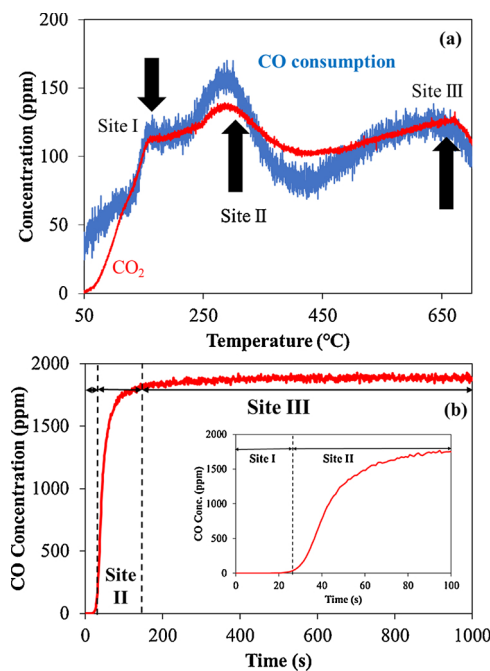


Fig. 4. (a) CO-TPR experiments [1000 ppm CO balance Ar at 10 °C/min], and (b) CO oxidation experiments [2000 ppm CO balance Ar at 400 °C] over the pre-oxidized catalyst.

(~2024 mol/m³_{WC} based on the known mass fraction of ceria) and the site concentrations of Site I + II. The site concentration values are shown in Table 1.

Once the loadings of the three site types were estimated, kinetic parameters for CO oxidation by stored oxygen were tuned using the CO effluent profiles. CO oxidized by the stored oxygen over three different sites were considered in this exercise. The reactions and rate expressions are provided in Table S-2. Fig. 5 shows a comparison of experimental and model-predicted CO effluent concentrations during the first 200 s of CO exposure. The model predicts the CO effluent profiles at three different temperatures. With increasing feed temperature, the stored oxygen activity shows a strong dependence on temperature. Especially for oxygen stored on Site I, at T_f = 250 °C, CO breakthrough at ~5 s, but, at T_f = 300 °C, the breakthrough time increases to ~10 s. In addition, Fig. 5c shows that the CO depletion lasts for ~25 s which suggests the ceria provides a significant impact on surface oxygen concentration and reductant oxidation reactions. However, Site III shows less participation during the first 200 s. For this reason, only Site types I and II were included in the cyclic modeling.

4.3. CO oxidation kinetics

Oxidation of feed components H₂, CO and HC_s is a key role of the TWC. During the cyclic lean-rich feed to the TWNSC the reduction of NO_x by H₂, CO and HC_s competes with their oxidation by both gas phase O₂ and oxygen stored on ceria. In order to accurately predict the extent of oxidation under transient conditions, CO temperature-programmed oxidation (TPO) experiments were conducted to estimate the CO oxidation kinetics over the model TWNSC. The CO oxidation kinetic model was developed following the global Langmuir-Hinshelwood model developed by Raj et al. [39]. The model considers that surface reaction between adsorbed CO and adsorbed O₂ occurs at a rate given by

$$R_{CO} = \frac{k_{13} X_{wc,O_2} X_{wc,CO} C_{PGM}}{G}, \quad (22)$$

where G = (1 + K_{CO}X_{wc,CO})². This semi-empirical rate expression

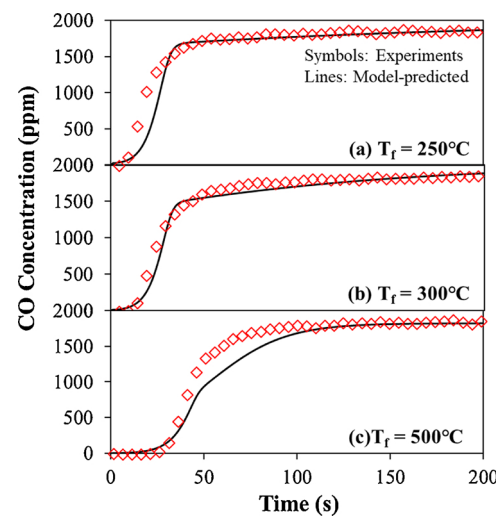


Fig. 5. Comparison of experimental and model-predicted effluent CO concentration profile over a pre-oxidized catalyst at (a) 250 °C, (b) 300 °C, (c) 500 °C. Symbols: experiments; Lines: model-predicted [Condition: CO = 2000 ppm and balance Ar].

follows the experimentally-observed reaction order with respect to CO in the low pressure (+1) and CO inhibition (-1) regimes [34,53]. However, it is noted that this kinetic model does not explicitly account for a role of ceria in CO oxidation. We return to this point below.

Fig. 6a shows the predicted light-off curve for CO oxidation for a feed containing 0.5% CO and O₂ with a 3 °C/min temperature ramp. The light-off curves, which have the classical sigmoidal shape, show that CO is fully converted by 200 °C. The fit was obtained using estimates for A_{T-1} and E_{T-1} of 7.15 × 10¹⁸ 1/s and 105 kJ/mol (Table S-3), respectively, comparing to values from Raj et al. [32] values of 1.28 × 10²¹ 1/s and 119.9 kJ/mol. The difference is attributed in part to catalyst composition differences in each study. In particular, the Pt/Al₂O₃ catalyst consists of 95 g/ft³ Pt loading which is somewhat higher than the TWNSC Pt loading. The model was tested at two lower CO feed concentrations of 2000 and 1000 ppm (Fig. 6b). While the model captures the CO self-inhibition with increasing CO concentration, the model under predicts the lower temperature conversion for these two cases.

As mentioned above, this kinetic model does not include a role of ceria in the oxidation which points to a reason for the under-prediction at lower temperature, conditions for which CO is inhibiting. Gorte et al. [54] compared CO oxidation over Rh/Al₂O₃ and Rh/Ceria and reported rate enhancement by the ceria. The ceria support provides an alternative CO oxidation pathway that results in a lower activation energy and higher reaction order in CO. Hoang et al. [55] found that ceria promotes propene oxidation through the oxygen spillover process resulting in a higher heat generation and propene consumption. The current global kinetic model was modified by accounting for the oxygen uptake on ceria and reaction with CO. Oxygen storage and surface oxygen reduction by CO over three oxygen storage sites (Reactions T-2 - T-7 provided in Table S-3) were incorporated in the global kinetic model to resolve the under prediction of CO conversion in CO TPO simulations. Fig. 7a shows the much-improved model-predicted CO light-off curves for 5000, 2000, and 1000 ppm CO feed concentrations. The schematic above Fig. 7a depicts that the addition of ceria provides stored oxygen for reaction with adsorbed CO at the PGM - ceria interface, mitigating the CO self-inhibition effect. However, after the depletion of stored oxygen, the CO self-inhibition still exists when increasing the feed concentration.

The impact of NO on CO oxidation must be considered given the known inhibitory features of NO. Voltz et al. [53] demonstrated the mutual inhibition of CO and NO over Pt sites and proposed a semi-

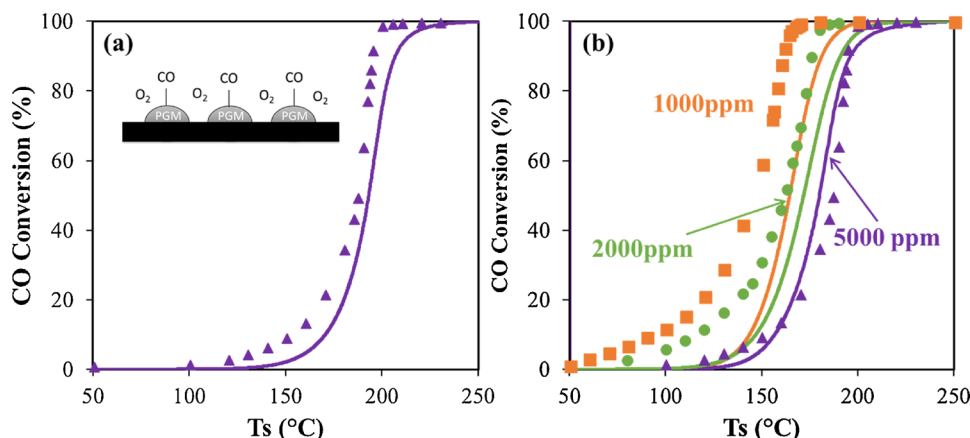


Fig. 6. (a) Fitted light-off curve of CO oxidation (b) model predicted light-off curve of CO at different CO concentration. Symbols: experiments; Lines: model-predicted [Conditions: 0.5% CO or 0.2% CO or 0.1% CO, 0.5% O₂ and balance Ar; temperature ramp: 3 °C/min].

empirical Langmuir-Hinshelwood rate expression. In the current study, 500 ppm NO was added to the CO and O₂ mixture to evaluate the CO and NO mutual inhibition during CO TPO experiments. Fig. 7b compares the CO conversion without and with NO in the feed. Clearly, the additional 500 ppm NO has an inhibiting effect on the CO light-off curve, with the T₅₀ increasing by ~30 °C compared to the CO-only feed. To account for this feature, a NO inhibition term was added to the denominator of the rate expression:

$$H = (1 + K_{CO}X_{wc,CO})^2(1 + K_{NO}X_{wc,NO}) \quad (23)$$

Furthermore, in order to account for NO inhibition in the CO TPO model, the NO oxidation, N₂ formation and N₂O formation reactions (Reaction T-8 – T-10) were incorporated. The parameters A_{T-8} and E_{T-8} were adjusted to fit the CO + NO co-oxidation model from the previous NOx storage model. Kinetic parameters of T-9 were adopted from TWC model developed by Ramanathan et al. [34]. A_{T-10}, and E_{T-10} were estimated from the experiment results shown in Fig. 8a. The parameter values are listed in Table S-3.

A comparison of experimental and model-predicted reactant conversions and product yields of CO TPO reactions are shown in Fig. 8. NO is selectively converted to N₂, N₂O, and NO₂. For T_s = 100–250 °C, N₂O and N₂ are the primary products while at higher temperature (T_s > 350 °C), NO₂ is the main product from NO oxidation. N₂O formation occurs after CO light-off and vanishes as CO conversion approaches 100%. While NO₂ breakthrough occurred at T_s = 250 °C and

exhibits a maximum NO₂ formation at 380 °C, which is consistent with NO oxidation in Fig. 2. The model-predicted CO conversion shown in Figs. 7b and 8 capture the main trends, however, the model under-predicts the CO conversion at higher temperatures and over predicts N₂O formation at lower temperatures. The discrepancy is the result of the generation of N₂O and its sensitivity to the O₂ concentration. Therefore, reaction step T-10 was not incorporated in the main TWNSC model. A more detailed NO + CO microkinetic model is under development in order to accurately capture the CO light-off, CO and NO mutual inhibition and N₂O formation.

4.4. Experiments and parameter estimation: steady-state conditions

In our previous work [1], the model TWNSC was evaluated under steady-state conditions. The above-described kinetic blocks were integrated to comprise the TWNSC kinetic model which was incorporated into a nonisothermal TWNSC reactor model to assess, among various features, NOx reduction and NH₃ generation over a range of feed compositions. Fig. 9 compares the experimental and model-predicted results over a range of feeds spanning rich and lean, for which the stoichiometric number (S_N) is within the range of 0.9 and 1.15 and the feed temperature is fixed at 270 °C. The experiments were carried out using 1% CO, 3300 ppm H₂ and 1000 ppm C₃H₆ as the reductant mixture with 1000 ppm C₃H₆ was converted to the equivalent amount of H₂ and CO in the model following an approach suggested by Kumar et al.

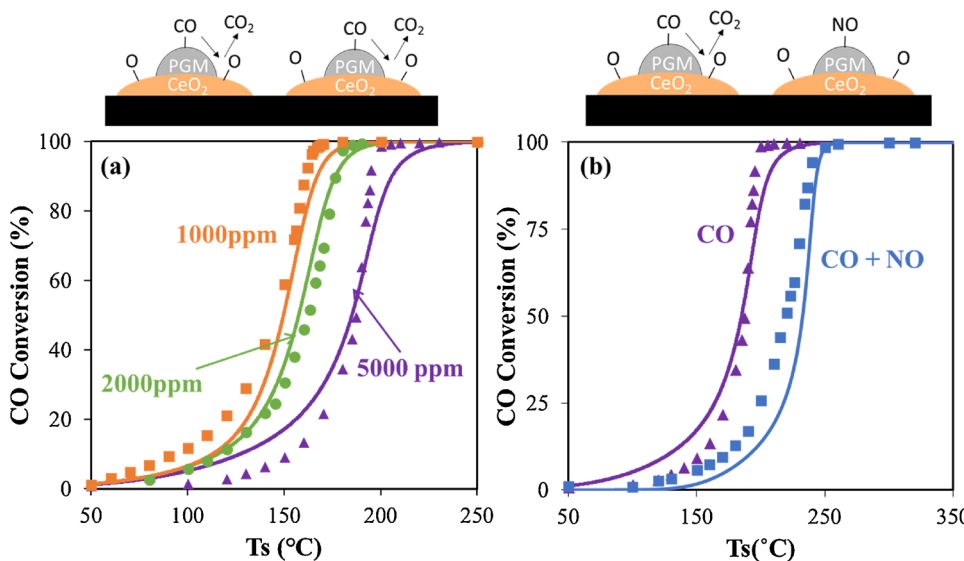


Fig. 7. (a) Modified model predicted light-off curve of CO oxidation at varied CO concentration [Conditions: 0.5% CO or 0.2% CO or 0.1% CO, 0.5% O₂ and balance Ar; temperature ramp: 3 °C/min] (b) Model-predicted light-off curve of CO w/ or w/o NO. Symbols: experiments; Lines: model-predicted [Conditions: 0.5% CO, 500 ppm NO, 0.5% O₂ and balance Ar; temperature ramp: 3 °C/min].

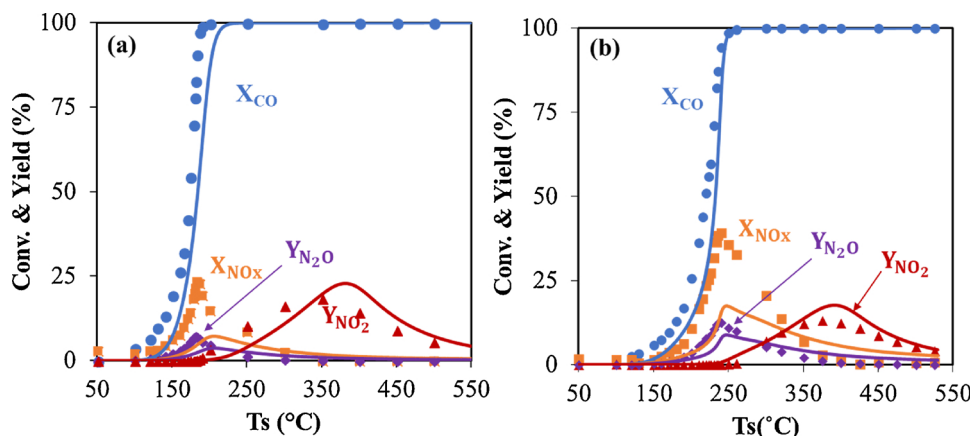


Fig. 8. Comparison of experimental and model-predicted reactant conversions and product yields from CO + NO TPO under conditions of (a) 2000 ppm CO or (b) 5000 ppm CO, with 500 ppm NO, 0.5% O₂ and balance Ar at ramp rate 3 °C/min. Symbols: experiments; Lines: model-predicted.

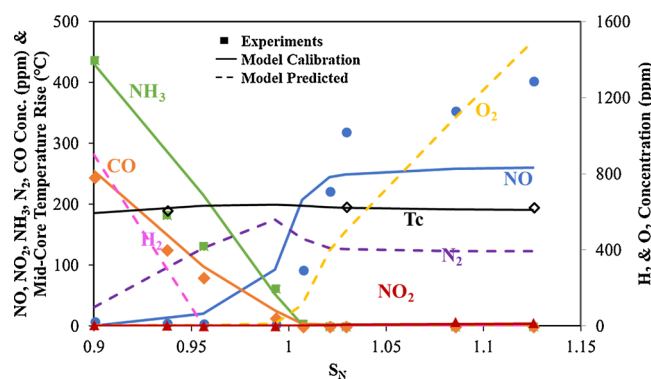


Fig. 9. Comparison of experimental and model-predicted results of steady-state species effluent concentrations (NO, NO₂, NH₃, N₂ and CO) and mid-core catalyst temperature rise as a function of the stoichiometric number at $T_f = 270$ °C. [Condition: 500 ppm NO, 1.6% CO, 6300 ppm H₂, 7% H₂O, 10% CO₂, 0.98–1.25% O₂ and balance Ar].

[44]. This gives a model feed gas consisting of 500 ppm NO, 1.6% CO, 6300 ppm H₂, 7% H₂O, 10% CO₂, 0.98–1.25% O₂ and balance Ar.

Table 5 lists the estimated kinetic parameters for steady-state operation; included are the sources of parameter values for Steps (R1) – (R25). Before describing the steady state model tuning, some iteration was done in concert with the cyclic model tuning, described in more detail below. With the objective to obtain a single set of parameters, this inevitably led to a compromise result. Steps (R1) – (R4) comprise

the reaction scheme for NO oxidation and NO_x storage. A subset of kinetic parameters (A_{T-8}, E_{T-8}, A_{N-2}, and A_{N-4}) retain their original values from the sub-models. Kinetic parameters for stored NO_x reduction (R5 – R8) are adopted from Shakya et al. [42]. Model tuning of the pre-exponential factors for NH₃ generation (R9) and consumption (R10–11) was conducted to converge on values resulting in an adequate fit of the NH₃ and NO effluent concentrations. The chemistries of H₂ oxidation (R13), NO_x reduction (R15 and R16), water gas shift reaction (R17) and ceria oxidation and reduction (R18 – R25) were adopted from the TWC model of Ramanathan et al. [34]. The pre-exponential factor for H₂ oxidation (R13) was estimated using the steady-state model. The pre-exponential (A₁₄) and activation energy (E₁₄) for CO oxidation (R14) were adjusted upon integrating the CO oxidation sub-model into the overall TWNSC steady-state model. Kinetic parameters for Steps (R15)–(R17) were fixed at the values provided by Ramanathan et al. [34]. Steps (R21) and (R25) comprise CO oxidation by stored oxygen on two oxygen storage sites (Sites I and II) with associate parameters estimated in the oxygen storage and reduction sub-model (O-1 and O-2); The kinetic parameters for ceria oxidation by NO or O₂ over two oxygen storage sites (Site I and Site II) were set equal as an approximation (i.e., A₁₈ = A₂₂, E₁₈ = E₂₂, A₁₉ = A₂₃, E₁₉ = E₂₃). In all, seven pre-exponential factors (A₉ – A₁₄, A₂₀ = A₂₄) were tuned to achieve a satisfactory fit of the steady-state data.

The model-predicted results capture the effluent concentrations for nine different feed compositions in the aforementioned S_N range (Fig. 9). By sweeping S_N from the rich to lean regime, the NO and NH₃ effluent concentrations vary significantly. In the rich regime ($S_N < 1$), NO_x is converted by the reductants including the generated NH₃. At

Table 5
Kinetic parameters used for TWNSC steady-state model.

#	A (1/s)	E (kJ/mol)	H _{rxn} (kJ/mol)	#	A (1/s)	E (kJ/mol)	H _{rxn} (kJ/mol)
1	3.8×10^4	24.49	-57	14	2.9×10^{19}	121.45 [34]	-373
2	3.7×10^7	0 [42]	-255	15	5.29×10^9	69.237 [34]	-242
3	1.2×10^3	0 [42]	-151	16	1.92×10^8	52.274 [34]	-283
4	3.63×10^7 [42]	140.1 [42]	-625	17	1.21×10^4	56.72 [34]	-41
5	4.42×10^7 [42]	60 [42]	-101	18	4.9×10^1	5.296 [34]	-200
6	2.61×10^{10} [42]	100 [42]	-101	19	2.64×10^2 [34]	25.101 [34]	-190
7	4.14×10^8 [42]	55 [42]	-613	20	2.78×10^2	26.816	-142
8	2.47×10^{22}	250 [42]	-613	21	8.35×10^2	14.816	-183
9	2.61×10^{18}	128.6 [42]	-378	22	4.91×10^1	5.296 [34]	-200
10	1.25×10^{14}	91.1 [42]	-452	23	2.64×10^2 [34]	25.101 [34]	-190
11	1.1×10^{20}	154.6 [35]	-226	24	2.78×10^2	14.816	-142
12	2.28×10^{12}	85 [42]	-340	25	3.42×10^3	30.793	-183
13	1.21×10^{17}	111.45 [34]	-332				

$S_N = 0.9$, ~450 ppm NH₃ is generated which corresponds to a N yield of 90%. This shows that the TWNSC is suitable for generating NH₃ needed for downstream SCR conversion of unconverted NO_x during cyclic operation. An increase in S_N through the stoichiometric neutral point ($S_N = 1$) results in a sharp increase in unconverted NO which is predicted adequately by the model. This increase underscores the failure of the TWNSC to catalytically reduce NO under lean conditions. The model predicts the N₂ concentration local maximum (~150 ppm) at $S_N \sim 0.98$; the maximum is expected given the combination of a declining NH₃ selectivity and NO conversion. The model predicts well the measured temperature rise along the monolith length, which approaches ~200 °C, indicating that thermal effects are significant. The model under predicts the unreacted NO in the lean regime. Attempts were made with limited success to improve the fit of these data points while obtaining a good fit of the cyclic data.

A benefit of the detailed modeling is the ability to examine predicted spatial profiles of the reacting species. Fig. 10 shows the model-predicted axial species concentration profiles at four selected feed gas conditions ($S_N = 0.9$, 0.993, 1.029, and 1.125) and a feed temperature of 270 °C. For the richest feed ($S_N = 0.9$), nearly all the NO is converted to NH₃ and the NH₃ concentration increases along the monolith reactor (Fig. 10a). For S_N slightly less than unity (0.993) the NH₃ concentration exhibits a local maximum located in the front one-third of the monolith (Fig. 10b). The maximum shows that NH₃ is generated by NO and H₂ in the front section and consumed downstream by its reaction with NO and O₂. It is interesting to note that even under the lean conditions in Fig. 10c and d, for which the effluent NH₃ concentration is zero, NH₃ is generated upstream. This feature is due to the local rich condition within the washcoat. We elaborate on this point below.

In Fig. 10, the corresponding NO concentration profile exhibits a local minimum due to the complex chemistry of NH₃ generation and consumption. The majority of NO is converted to NH₃ by H₂ (R9) in the front portion of TWNSC. However, downstream the NH₃ reacts with NO or O₂ generating N₂ and NO. The imbalance in NO consumption and formation within the TWNSC creates the local NO minimum profile. The local NH₃ maximum and local NO minimum are a result of the

coupled chemistry spanning reductant oxidation, NOx reduction, and NH₃ formation and consumption at the front section of TWNSC. While in the rear section of the TWNSC, less reductant is available for NOx reduction and NH₃ formation, and more O₂ is available for NH₃ consumption. At $S_N = 0.9$, most of the NO converted to NH₃. The model-predicted N₂ also shows the highest yield for $S_N \sim 1$.

It is instructive to examine NH₃ generation in more detail. Fig. 11a shows the dependence of the NH₃ washcoat concentration as a function of axial position for a wide range of feed S_N values (0.5–4.48). Only the leanest feed shows a monotonically declining NH₃ concentration. For all $S_N < 1.13$, the NH₃ concentration sharply increases in the front section of the monolith with its downstream value increasing with decreasing S_N . We define the washcoat stoichiometric number as

$$S_{N,wc} = \frac{2X_{wc,O_2} + X_{wc,NO}}{X_{wc,H_2} + X_{wc,CO}} \quad (24)$$

The $S_{N,wc}$ axial profiles show a local minimum. In the front of the reactor $S_{N,wc}$ moderately decreases then sharply increases downstream. Interestingly, the two moderately lean feeds ($S_N = 1.029, 1.125$) exhibit net rich mixtures within the washcoat in the front section of the monolith. For example, for $S_N = 1.029$, $S_{N,wc}$ reaches a value as low as ~0.8 at the 3 mm point.

These features are the result of differences in the extent of washcoat diffusion limitations as shown by the fluid and washcoat phase species concentrations profiles. The model-predicted axial dimensionless fluid and washcoat concentration profiles for NO ($= \frac{X_{wc,f,NO}}{X_{NO,feed}}$), NH₃ ($= \frac{X_{wc,f,NH_3}}{X_{NO,feed}}$), H₂, CO and O₂ ($= \frac{X_{wc,f,i}}{X_{feed,i}}$, i = H₂, CO and O₂) at $S_N = 0.5$, 0.993, 1.029, and 4.48 are shown in Fig. 12. The axial profiles show that NH₃ generation results from the comparatively plentiful supply of H₂ which creates the net rich environment. A comparison of the H₂ and O₂ concentrations for the $S_N = 1.029$ feed (Fig. 12f) shows a much higher H₂ concentration than O₂ which is nearly depleted in the front section. The much faster diffusion of H₂ compared to the other reacting species (CO, O₂, NH₃) creates the localized rich conditions which favor NH₃ production. The corresponding NH₃ profiles show a higher

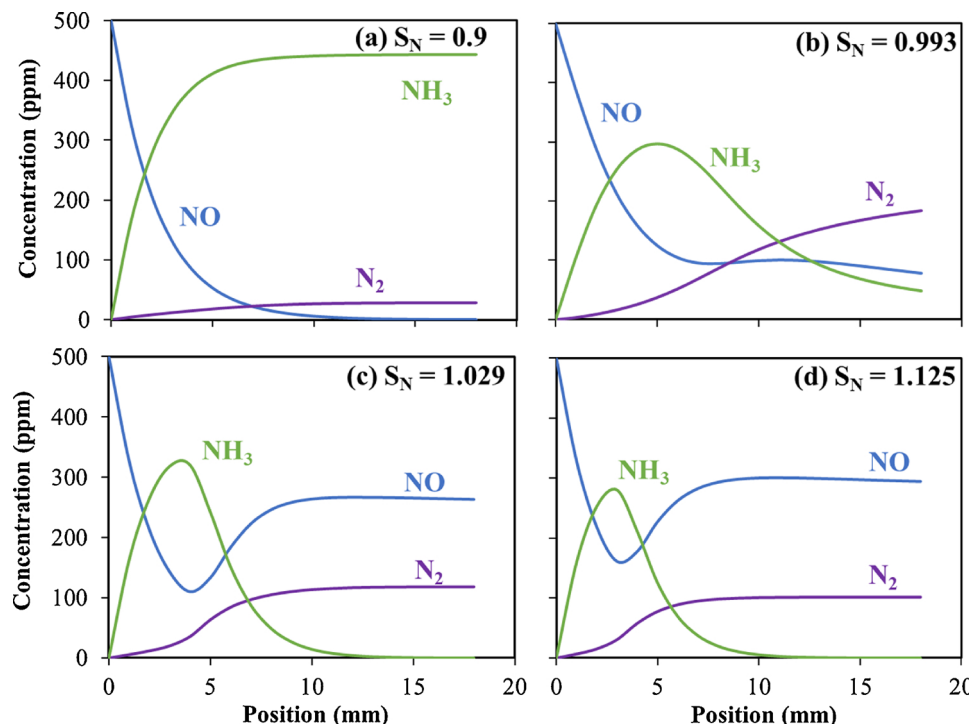


Fig. 10. Model-predicted axial NO, NH₃, and N₂ concentrations profile at (a) $S_N = 0.9$, (b) $S_N = 0.993$, (c) $S_N = 1.029$, and (d) $S_N = 1.125$ at $T_f = 270$ °C. [Condition: 500 ppm NO, 1.6% CO, 6300 ppm H₂, 7% H₂O, 10% CO₂, 0.98–1.25% O₂ and balance Ar].

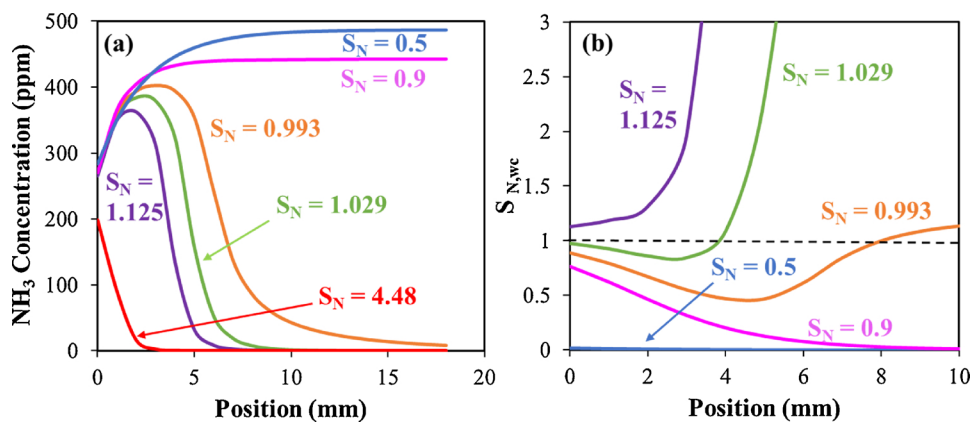


Fig. 11. Model-predicted axial washcoat phase (a) NH_3 concentration and (b) $S_{N,wc}$ value profile at $T_f = 270^\circ\text{C}$. [Condition: 500 ppm NO, 1.6% CO, 6300 ppm H_2 , 7% H_2O , 10% CO_2 , 0.98–1.25% O_2 and balance Ar].

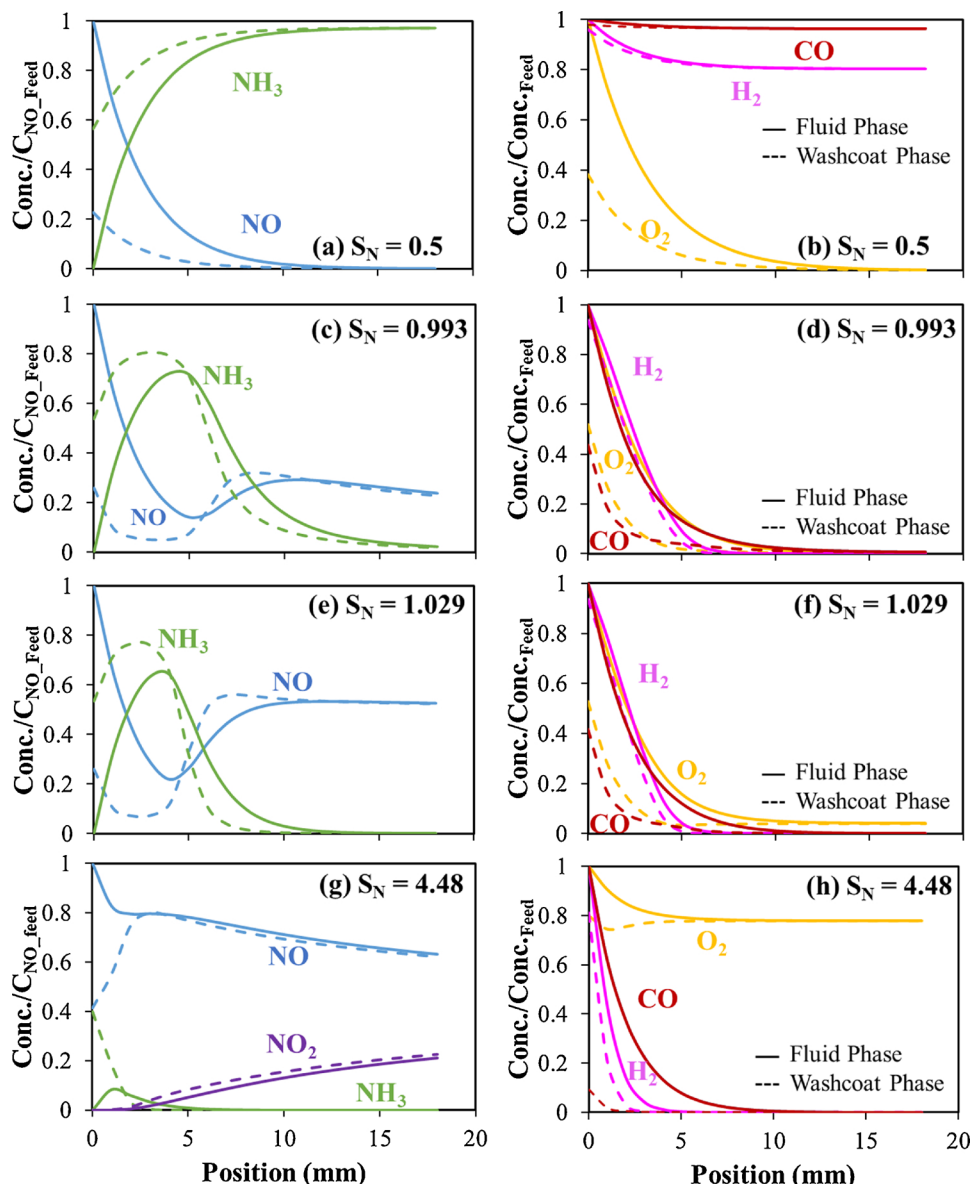


Fig. 12. Model-predicted dimensionless fluid (solid lines) and washcoat (dash lines) NO , NH_3 axial concentrations (left column) and CO , H_2 and O_2 axial concentrations (right column) at $S_N = 0.5$, $S_N = 0.993$, $S_N = 1.029$, and $S_N = 4.48$ at $T_f = 270^\circ\text{C}$. [Condition: 500 ppm NO, 1.6% CO, 6300 ppm H_2 , 7% H_2O , 10% CO_2 , 0.98–1.25% O_2 and balance Ar].

washcoat than fluid phase concentration in the front section with NH_3 diffusing out of the washcoat while downstream there is a net diffusion of NH_3 into the washcoat.

In comparison, the profiles for the rich feed ($S_N = 0.5$; Fig. 12a and b) show that NH_3 is generated along the entire length with the washcoat NH_3 concentration exceeding the fluid phase concentration. For the much leaner feed ($S_N = 4.48$, Fig. 12g), very little NH_3 formation is observed at the entrance. The decrease of NO along the length is a result of NO oxidation to NO_2 . A subtle but interesting feature is seen for near stoichiometric feeds for which the NO washcoat concentration slightly exceeds the NO fluid concentration, indicating a net generation of NO; e.g. see Fig. 12e. This is a result of NH_3 oxidation.

Collectively, these results point to the importance of sizing the TWNSC for either NO reduction to N_2 or NH_3 formation depending on the application. In the TWNSC + SCR application, a balance is needed between unconverted NO_x and generated NH_3 . The profiles help to pinpoint the reactor length needed to approach that balance to generate sufficient NH_3 .

4.5. Experiments and parameter estimation: cyclic operation

A comparison of model-predictions and experimental data is shown in Fig. 13 over a wide range of total cycle times (TCT, 0–200 s). The duty cycle rich (DCR) is fixed at 50% and feed temperature at 270 °C. Shown is the cycle-averaged NO_x and CO conversions, NH_3 selectivity and ANR as a function of TCT. The model predicts well most of the experimental trends. Key features of the plot are highlighted.

The NO_x conversion exhibits a maximum at an intermediate cycle time. The experimental value of 86% at TCT = 22 s compares to the model-predicted values of 82% and 30 s, respectively. A NO_x conversion versus cycle time maximum was first reported for a LNT by Kabin et al. [56] (using propylene as the reductant) and more recently was corroborated by Malamis et al. [1] for the TWNSC using $\text{CO} + \text{H}_2$ and $\text{CO} + \text{H}_2 + \text{C}_3\text{H}_6$ mixtures. The location and magnitude of the maximum depend on several factors, including the DCR value, rich feed composition, and temperature. The limiting behaviors at short and long TCT correspond to the mixed feed conversion for $\text{TCT} \rightarrow 0$ and weighted average NO_x conversion for $\text{TCT} \rightarrow \infty$ [1]. The maximum itself is a manifestation of the utilization of NO_x storage sites. Too short a cycle time prevents the regeneration of NO_x storage sites due to the net lean atmosphere. A recent LNT model developed by Ting et al. [45] explicitly accounts for upstream mixing of lean and rich feeds. Too long a cycle leads to excessive NO_x breakthrough during the lean part of the cycle.

The NH_3 selectivity is an increasing function of TCT. In turn, the

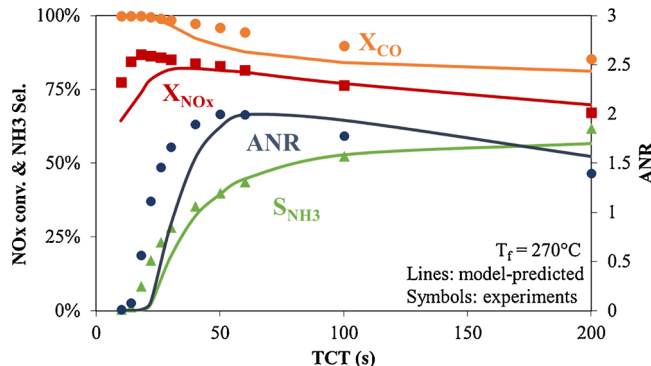


Fig. 13. Comparison of experimental and model-predicted cycle-averaged NO_x conversion, NH_3 selectivity and ANR as a function of TCT over TWNSC at $T_f = 270$ °C. Symbols: experiment; Lines: model-predicted [Conditions: Lean ($S_N = 7.4$): 500 ppm NO, 1% CO, 3300 ppm H_2 , 7% H_2O , 10% CO_2 , 5% O_2 ; Rich ($S_N = 0.49$): 500 ppm NO, 1% CO, 3300 ppm H_2 , 7% H_2O , 10% CO_2 , 0.3% O_2 at DCR 50%].

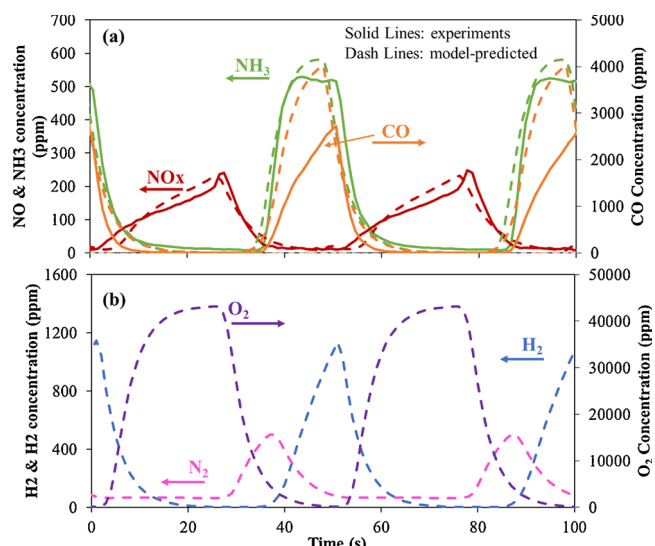


Fig. 14. (a) Comparison of experimental and model-predicted transient NO_x , NH_3 and CO concentrations and (b) model-predicted transient H_2 , N_2 and O_2 concentrations over TWNSC at $\text{TCT} = 50$ s and $T_f = 270$ °C. Solid lines: experiment; Dash lines: model-predicted [Conditions: Lean ($S_N = 7.4$): 500 ppm NO, 1% CO, 3300 ppm H_2 , 7% H_2O , 10% CO_2 , 5% O_2 ; Rich ($S_N = 0.49$): 500 ppm NO, 1% CO, 3300 ppm H_2 , 7% H_2O , 10% CO_2 , 0.3% O_2 at DCR 50%].

ANR itself exhibits a maximum at a slightly higher TCT than the NO_x conversion. The ANR maximum is a result of the combination of the increasing NH_3 selectivity and decreasing NO_x conversion. The model captures well each of these trends. The NH_3 selectivity increase with TCT conveys the benefit of a longer rich reduction of NO_x to NH_3 with decreasing downstream NH_3 consumption. In addition, a longer cycle leads to less oxygen storage on the ceria which would otherwise promote NH_3 oxidation. This helps to explain the decreasing trend of CO oxidation with TCT.

The predictive capability of the model is evident through comparison of experimental and model-predicted species concentrations during cyclic operation. Fig. 14 compares the effluent NO_x , NH_3 , and CO concentrations at $\text{TCT} = 50$ s. The model captures well the transient concentration profiles (Fig. 14a). Fig. 14b provides the model-predicted N_2 , O_2 , and H_2 effluent concentrations to assist in the interpretation. NO_x is stored at the beginning of the lean phase, which lasts for 25 s. A slow NO_x breakthrough is observed reaching a peak value of ~200 ppm. At 25 s, the rich feed is introduced, which leads to the rapid decrease in NO_x concentration. The model-predicted N_2 concentration shows a peak value during the early rich phase, suggesting N_2 is the primary product at early rich phase. After NO_x is depleted, N_2 formation decreases and NH_3 emerges as the primary product. Shortly thereafter NH_3 breaks through along with H_2 which corresponds to the point of complete regeneration. The NH_3 concentration approaches ~550 ppm, indicating that NH_3 is the major product by this point in the cycle. Upon switching to the lean feed, ~65 ppm N_2 is generated during the lean phase, which is the result of generated NH_3 reacting with NO_x in the front section of the TWNSC (see Fig. 10c and d). The model-predicted H_2 breakthrough from TWNSC during the late rich phase is consistent with the NH_3 generation.

Construction of time versus position storage site contour plots provides a detailed spatio-temporal characterization of the cyclic trends. Fig. 15 shows the model-predicted spatio-temporal NO_x storage site coverage profiles for $\text{TCT} = 10$ s (a, b) and 100 s (c, d) spanning one full cycle. The color bar represents the utilization of fast or slow NO_x storage sites with full utilization shown in red and no utilization shown in blue. During the first 5 s, the catalyst is exposed to a lean feed and the fast NO_x storage sites are rapidly filled along the entire monolith length. Upon switching to the rich feed, the NO_x storage sites are

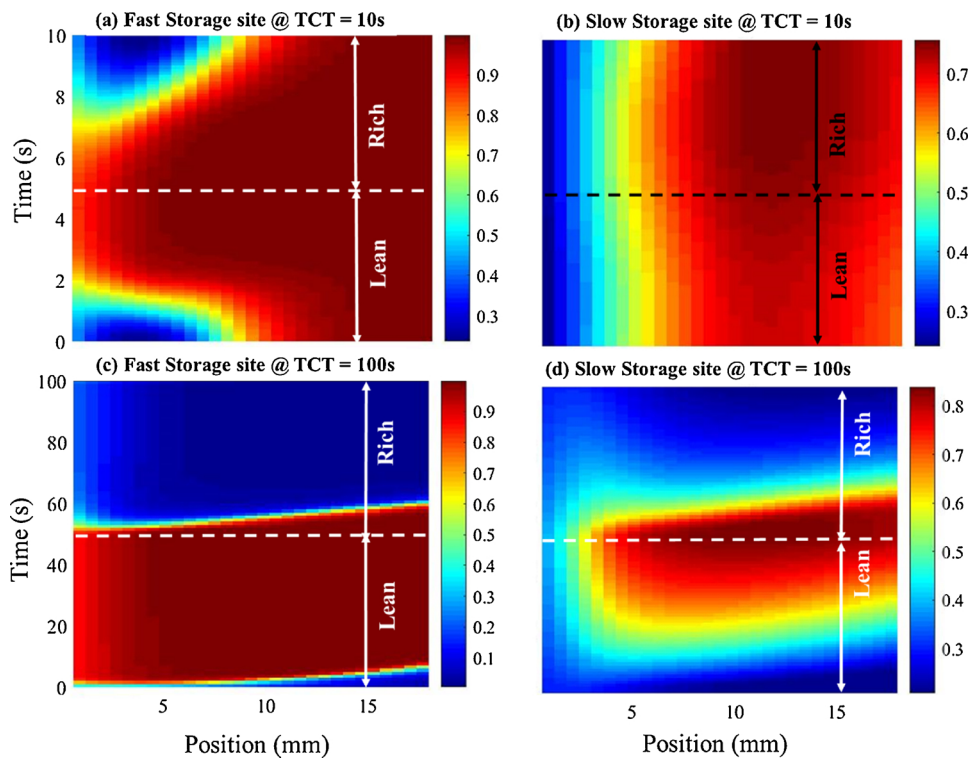


Fig. 15. Model-predicted spatio-temporal (a) fast and (b) slow NO_x storage sites coverage at TCT = 10 s and (c) fast and (d) slow NO_x storage sites coverage at TCT = 100 s. [Conditions: Lean ($S_N = 7.4$): 500 ppm NO, 1% CO, 3300 ppm H₂, 7% H₂O, 10% CO₂, 5% O₂; Rich ($S_N = 0.49$): 500 ppm NO, 1% CO, 3300 ppm H₂, 7% H₂O, 10% CO₂, 0.3% O₂ at DCR 50%].

rapidly regenerated during which time the stored NO_x is converted to NH₃ upstream, which reacts with stored NO_x downstream, producing N₂. For the TCT = 10 s case ~50% of the fast NO_x storage sites are regenerated in the first 8 mm while only ~10% of the fast NO_x storage sites are regenerated towards the end of the monolith. In contrast to the fast storage sites, the slow storage sites are less utilized, particularly in the front section, while nearly ~70% of slow NO_x storage sites are utilized at the back end of the catalyst. The regeneration of slow NO_x

storage sites is much slower during the short rich phase. The longer cycle time predictions shown in Fig. 15c and d indicate a better utilization of the storage sites, albeit less efficient. The protracted 50 s regeneration is much longer than is needed; e.g. the fast storage sites are sufficiently regenerated after 15 s. This shows that the rich period could be shortened in order to reduce the amount of reductant required.

As mentioned earlier, the heat effects can be appreciable and must be accounted for or performance data will be misinterpreted. Fig. 16

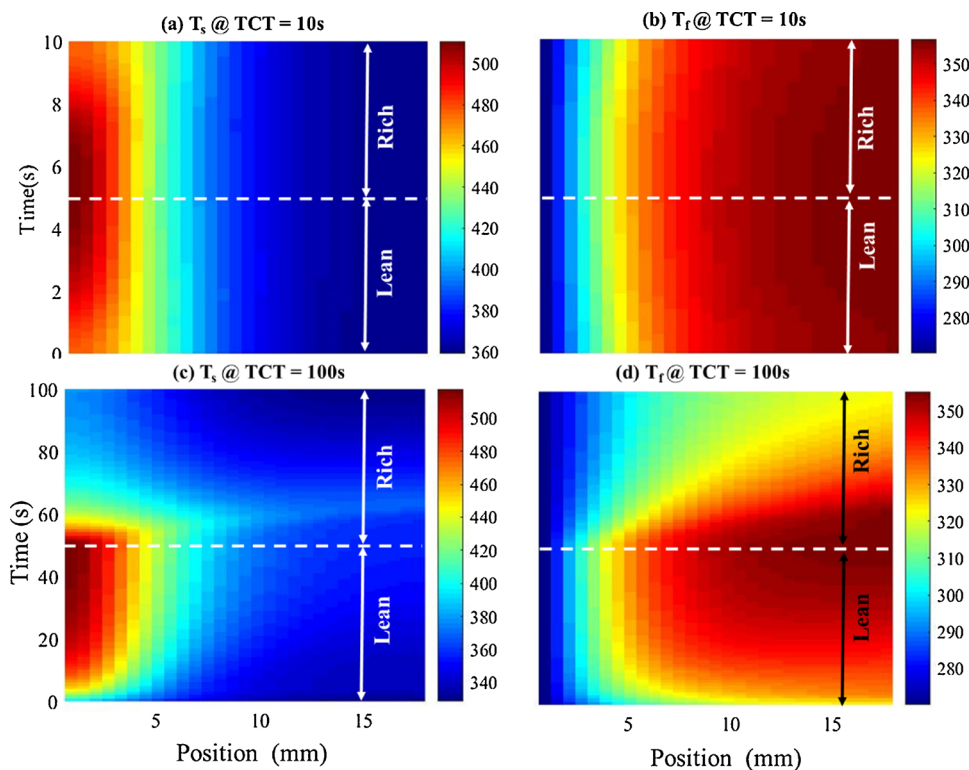


Fig. 16. Model-predicted spatio-temporal (a) solid and (b) fluid temperature at TCT = 10 s and (c) solid and (d) fluid temperature at TCT = 100 s. [Conditions: Lean ($S_N = 7.4$): 500 ppm NO, 1% CO, 3300 ppm H₂, 7% H₂O, 10% CO₂, 5% O₂; Rich ($S_N = 0.49$): 500 ppm NO, 1% CO, 3300 ppm H₂, 7% H₂O, 10% CO₂, 0.3% O₂ at DCR 50%].

shows the model-predicted spatio-temporal solid and fluid temperature profiles for TCT = 10 s (a, b) and 100 s (c, d) spanning one full cycle. The shorter cycle shows that the temperature rise at the exit of the monolith is nearly constant throughout the 10 s cycle. However, the spatial temperature profile shows a rather sharp distribution. Clearly, most of the reductant is consumed resulting in significant heat generation in the front ~20% of the monolith length. The solid temperature decreases along the length while the fluid temperature increases. The longer cycle time shows considerable more variation of the temperature with time. During the lean part of the cycle, ignition occurs with the concomitant increase in the catalyst temperature. Local cooling occurs during the rich part of the cycle as O₂ is depleted. Undoubtedly, the large variations in the temperature impact the TWNSC performance.

5. Conclusions

In this study, we have developed a TWNSC monolithic reactor model for the lean-burn gasoline application. The model combines the relevant mass and heat transport processes with a global kinetic description of the chemistry. The model captures most of the experimental trends in the performance of a model TWNSC reported by Malamis et al. [1]. A systematic method was followed in the development and parameter estimation of the main underlying catalytic reaction, NO_x storage, and O₂ storage processes. The process involved a combination of specific steady-state and transient experiments designed to estimate kinetic parameters. In order to balance the NO_x storage functionality and TWC functionality, several sub-models were developed, i.e., NO oxidation and NO_x storage model, oxygen storage model, and CO light-off kinetics, based on the kinetic experiments, i.e., NO oxidation and NO_x uptake experiments, CO-TPR and CO oxidation experiments, and CO-TPO, respectively. A dual NO_x storage site model and a triple oxygen storage site model were developed based on the experiments of NO_x uptake and CO oxidation with stored oxygen. The CO TPO model was developed to capture the CO light-off trend included CO and NO mutual inhibition effects. Afterward, these sub-models were combined together for NO_x reduction and NH₃ generation prediction at steady-state and cyclic conditions. According to the model prediction under the steady-state condition, the TWNSC model is capable of capturing the effluent trend spanning a range of S_N. The cyclic model could capture the cycle-averaged NO_x and CO conversions, NH₃ generation and ANR through a wide range of TCT and the transient species profiles at TCT = 50 s. Model-predicted spatio-temporal profiles of NO_x storage sites coverage and solid and fluid temperature profiles significantly enhance the understanding of dynamic NO_x storage profiles and non-isothermal features within TWNSC monolith, which provides information for catalyst design and optimization.

Finally, the TWNSC model provides a useful tool for evaluation of TWNSC catalyst performance spanning a wide range of operation conditions which can assist the optimization of catalyst design and operation strategies for the standalone TWNSC and TWNSC + SCR configuration.

Acknowledgements

The authors would like to thank FCA US LLC for financial support along with the fruitful discussions with Kiran Premchand, Craig Dimaggio, Vence Easterling, and Yang Zheng.

Appendix A. Supplementary data

Supplementary material related to this article can be found, in the online version, at doi:<https://doi.org/10.1016/j.apcatb.2018.09.094>.

References

- [1] S.A. Malamis, M. Li, W.S. Epling, M.P. Harold, C. Dimaggio, K. Premchand, Steady state and lean-rich cycling characterization of a three-way NO_x storage catalyst (TWNSC), *Appl. Catal. B Environ.* 237 (2018) 588–602.
- [2] W.S. Epling, L.E. Campbell, A. Yezerski, N.W. Currier, J.E. Parks, Overview of the fundamental reactions and degradation mechanisms of NO_x storage/reduction catalysts, *Catal. Rev.* 46 (2004) 163–245, <https://doi.org/10.1081/CR-200031932>.
- [3] M.P. Harold, NO_x storage and reduction in lean burn vehicle emission control: a catalytic engineer's playground, *Curr. Opin. Chem. Eng.* 1 (2012) 303–311, <https://doi.org/10.1016/j.coche.2012.02.002>.
- [4] S. Brandenberger, O. Kröcher, A. Tissler, R. Althoff, The state of the art in selective catalytic reduction of NO by ammonia Using metal-exchanged zeolite catalysts, *Catal. Rev.* 50 (2008) 492–531, <https://doi.org/10.1080/01614940802480122>.
- [5] J. Guenther, B. Konrad, B. Krutzsch, A. Nolte, D. Voigtlaender, M. Weibel, et al., US6338244B1, 1999.
- [6] R.H. John Cavataio, Yisun Cheng, Haren Gandhi, US20040076565, 2004.
- [7] J.R. Theis, M. Dearth, R. McCabe, LNT+SCR catalyst systems optimized for NO_x conversion on diesel applications, *SAE Tech. Pap.* (2011) 2011-01-03.
- [8] Y. Zheng, Y. Liu, M.P. Harold, D. Luss, LNT-SCR dual-layer catalysts optimized for lean NO_x reduction by H₂ and CO, *Appl. Catal. B Environ.* 148–149 (2014) 311–321, <https://doi.org/10.1016/j.apcatb.2013.11.007>.
- [9] Y. Liu, M.P. Harold, D. Luss, Coupled NO_x storage and reduction and selective catalytic reduction using dual-layer monolithic catalysts, *Appl. Catal. B Environ.* 121–122 (2012) 239–251, <https://doi.org/10.1016/j.apcatb.2012.04.013>.
- [10] Y. Zheng, M. Li, M.P. Harold, D. Luss, Enhanced low-temperature NO_x conversion by high-frequency hydrocarbon pulsing on a dual layer LNT-SCR catalyst, *SAE Int. J. Engines.* 8 (2015) 1117–1125, <https://doi.org/10.4271/2015-01-0984>.
- [11] L. Xu, R. McCabe, M. Dearth, W. Ruona, Laboratory and vehicle demonstration of “2nd- generation” LNT + in-situ SCR diesel NO_x emission control systems, *SAE Int. J. Fuels Lubr.* 3 (2010) 37–49, <https://doi.org/10.4271/2010-01-0305>.
- [12] J. Wang, Y. Ji, Z. He, M. Crocker, M. Dearth, R.W. McCabe, A non-NH₃ pathway for NO_x conversion in coupled LNT-SCR systems, *Appl. Catal. B Environ.* 111–112 (2012) 562–570, <https://doi.org/10.1016/j.apcatb.2011.11.008>.
- [13] A. Lindholm, H. Sjövall, L. Olsson, Reduction of NO_x over a combined NSR and SCR system, *Appl. Catal. B Environ.* 98 (2010) 112–121, <https://doi.org/10.1016/j.apcatb.2010.05.019>.
- [14] L. Castoldi, R. Bonzi, L. Lietti, P. Forzatti, S. Morandi, G. Ghiorri, et al., Catalytic behaviour of hybrid LNT/SCR systems: reactivity and in situ FTIR study, *J. Catal.* 282 (2011) 128–144, <https://doi.org/10.1016/j.jcat.2011.06.002>.
- [15] M. Li, V.G. Easterling, M.P. Harold, Towards optimal operation of sequential reduction, NO_x storage and reduction and selective catalytic reduction, *Appl. Catal. B Environ.* 184 (2016) 364–380, <https://doi.org/10.1016/j.apcatb.2015.11.029>.
- [16] M. Li, V.G. Easterling, M.P. Harold, Spatio-temporal features of the sequential NO_x storage and reduction and selective catalytic reduction reactor system, *Catal. Today* 267 (2016) 177–191, <https://doi.org/10.1016/j.cattod.2016.01.020>.
- [17] C. Enderle, G. Vent, M. Paule, BLUETEC diesel technology - clean, efficient and powerful, *SAE Tech. Pap.* (2008), <https://doi.org/10.4271/2008-01-1182> 2008-01-1182.
- [18] C.H. Kim, K. Perry, M. Viola, W. Li, K. Narayanaswamy, Three-way catalyst design for ureless passive Ammonia scr: lean-burn SIIDI aftertreatment system, *SAE Tech. Pap.* (2011) 2011-01-0306.
- [19] C.D. DiGiulio, J.A. Pihl, J.E. Parks II, M.D. Amiridis, T.J. Toops, Passive-ammonia selective catalytic reduction (SCR): understanding NH₃ formation over close-coupled three way catalysts (TWC), *Catal. Today* 231 (2014) 33–45, <https://doi.org/10.1016/j.cattod.2014.01.027>.
- [20] J.R. Theis, J. Kim, G. Cavataio, Passive TWC+SCR systems for satisfying tier 2, bin 2 emission standards on lean-burn gasoline engines, *SAE int. J. Fuels Lubr.* 8 (2015) 460–473, <https://doi.org/10.4271/2015-01-1004>.
- [21] Y. Murata, T. Morita, K. Wada, H. Ohno, NO_x trap three-way catalyst (N-TWC) concept: TWC with NO_x adsorption properties at low temperatures for cold-start emission control, *SAE int. J. Fuels Lubr.* 8 (2015) 1–6, <https://doi.org/10.4271/2015-01-1002>.
- [22] E.C. Adams, M. Skoglundh, P. Gabrielsson, M. Laurell, P.-A. Carlsson, Ammonia formation over Pd/Al₂O₃ modified with cerium and barium, *Catal. Today* 267 (2016) 210–216, <https://doi.org/10.1016/j.cattod.2016.01.012>.
- [23] A. Güthenke, D. Chatterjee, M. Weibel, B. Krutzsch, P. Kočí, M. Marek, et al., Current status of modeling lean exhaust gas aftertreatment catalysts, *Adv. Chem. Eng.* 33 (2007), [https://doi.org/10.1016/S0065-2377\(07\)33003-2](https://doi.org/10.1016/S0065-2377(07)33003-2) 103–211–283.
- [24] M. Marek, P. Kočí, Overview of LNT modeling approaches, *CLEERS Work.* (2012).
- [25] D. Bhatia, M.P. Harold, V. Balakotaiah, Modeling the effect of Pt dispersion and temperature during anaerobic regeneration of a lean NO_x trap catalyst, *Catal. Today* 151 (2010) 314–329, <https://doi.org/10.1016/j.cattod.2010.02.055>.
- [26] B.M. Shakya, M.P. Harold, V. Balakotaiah, Crystallite-scale model for NO_x storage and reduction on Pt/BaO/Al₂O₃: Pt dispersion effects on NO_x conversion and ammonia selectivity, *Catal. Today* 184 (2012) 27–42, <https://doi.org/10.1016/j.cattod.2012.01.037>.
- [27] B.M. Shakya, M.P. Harold, V. Balakotaiah, Effect of cycle time on NH₃ generation on low Pt dispersion Pt/BaO/Al₂O₃ catalysts: experiments and crystallite-scale modeling, *Chem. Eng. J.* 230 (2013) 584–594, <https://doi.org/10.1016/j.cej.2013.06.109>.
- [28] B.R. Kromer, L. Cao, L. Cumaranatunge, S.S. Mulla, J.L. Ratts, A. Yezerski, et al., Modeling of NO oxidation and NO_x storage on Pt/BaO/Al₂O₃ NO_x traps, *Catal. Today* 136 (2008) 93–103, <https://doi.org/10.1016/j.cattod.2008.02.013>.
- [29] P. Kočí, F. Plát, J. Štěpánek, Š. Bártová, M. Marek, M. Kubíček, et al., Global kinetic

- model for the regeneration of NOx storage catalyst with CO, H₂ and C₃H₆ in the presence of CO₂ and H₂O, *Catal. Today* 147 (2009) S257–S264, <https://doi.org/10.1016/j.cattod.2009.07.036>.
- [30] P. Kočí, Š. Bártová, D. Mráček, M. Marek, J.S. Choi, M.Y. Kim, et al., Effective model for prediction of N₂O and NH₃ formation during the regeneration of NO x storage catalyst, *Top. Catal.* 56 (2013) 118–124, <https://doi.org/10.1007/s11244-013-9939-y>.
- [31] R.S. Larson, J.A. Pihl, V. Kalyana Chakravarthy, T.J. Toops, C.S. Daw, Microkinetic modeling of lean NOx trap chemistry under reducing conditions, *Catal. Today* 136 (2008) 104–120, <https://doi.org/10.1016/j.cattod.2007.12.117>.
- [32] D. Chatterjee, P. Kočí, V. Schmeißer, M. Marek, M. Weibel, B. Krutzsch, Modelling of a combined NOx storage and NH₃-SCR catalytic system for diesel exhaust gas aftertreatment, *Catal. Today* 151 (2010) 395–409, <https://doi.org/10.1016/j.cattod.2010.01.014>.
- [33] M. Weibel, N. Waldbüßer, R. Wunsch, D. Chatterjee, B. Bandl-Konrad, B. Krutzsch, A novel approach to catalysis for NO x reduction in diesel exhaust gas, *Top. Catal.* 52 (2009) 1702–1708, <https://doi.org/10.1007/s11244-009-9329-7>.
- [34] K. Ramanathan, C.S. Sharma, Kinetic parameters estimation for three way catalyst modeling, *Ind. Eng. Chem. Res.* 50 (2011) 9960–9979, <https://doi.org/10.1021/ie200726j>.
- [35] K. Ramanathan, C.S. Sharma, C.H. Kim, Global kinetics for ammonia formation and oxidation reactions in a commercial three-way catalyst, *Ind. Eng. Chem. Res.* 51 (2012) 1198–1208, <https://doi.org/10.1021/ie2017866>.
- [36] J. Gong, C. Rutland, Three way catalyst modeling with Ammonia and nitrous oxide kinetics for a lean burn spark ignition direct injection (SIDI) gasoline engine, *SAE Tech. Pap.* (2013) 2013-01-1572.
- [37] S.Y. Joshi, M.P. Harold, V. Balakotaiah, Low-dimensional models for real time simulations of catalytic monoliths, *AIChE J.* 55 (2009) 1771–1783, <https://doi.org/10.1002/aic>.
- [38] D. Bhatia, R.D. Clayton, M.P. Harold, V. Balakotaiah, A global kinetic model for NOx storage and reduction on Pt/BaO/Al₂O₃ monolithic catalysts, *Catal. Today* 147 (2009) 250–256, <https://doi.org/10.1016/j.cattod.2009.07.024>.
- [39] R. Raj, M.P. Harold, V. Balakotaiah, Steady-state and dynamic hysteresis effects during lean co-oxidation of CO and C₃H₆ over Pt/Al₂O₃ monolithic catalyst, *Chem. Eng. J.* 281 (2015) 322–333, <https://doi.org/10.1016/j.cej.2015.06.057>.
- [40] B.R. Bird, W.E. Stewart, E.N. Lightfoot, *Transport Phenomena*, 2nd editio, John Wiley & Sons, Inc., 2006.
- [41] K. Ramanathan, V. Balakotaiah, D.H. West, Light-off criterion and transient analysis of catalytic monoliths, *Chem. Eng. Sci.* 58 (2003) 1381–1405, [https://doi.org/10.1016/S0009-2509\(02\)00679-6](https://doi.org/10.1016/S0009-2509(02)00679-6).
- [42] B.M. Shakya, M.P. Harold, V. Balakotaiah, Modeling and analysis of dual-layer NOx storage and reduction and selective catalytic reduction monolithic catalyst, *Chem. Eng. J.* 237 (2014) 109–122, <https://doi.org/10.1016/j.cej.2013.10.008>.
- [43] S.Y. Joshi, M.P. Harold, V. Balakotaiah, On the use of internal mass transfer coefficients in modeling of diffusion and reaction in catalytic monoliths, *Chem. Eng. Sci.* 64 (2009) 4976–4991, <https://doi.org/10.1016/j.ces.2009.08.008>.
- [44] P. Kumar, T. Gu, K. Grigoriadis, M. Franchek, V. Balakotaiah, Spatio-temporal dynamics of oxygen storage and release in a three-way catalytic converter, *Chem. Eng. Sci.* 111 (2014) 180–190, <https://doi.org/10.1016/j.ces.2014.02.014>.
- [45] A.W.-L. Ting, M. Li, M.P. Harold, V. Balakotaiah, Fast cycling in a non-isothermal monolithic lean NOx trap using H₂ as reductant: experiments and modeling, *Chem. Eng. J.* (2017), <https://doi.org/10.1016/j.cej.2017.05.002>.
- [46] D. Bhatia, R.W. McCabe, M.P. Harold, V. Balakotaiah, Experimental and kinetic study of NO oxidation on model Pt catalysts, *J. Catal.* 266 (2009) 106–119, <https://doi.org/10.1016/j.jcat.2009.05.020>.
- [47] W.S. Epling, J.E. Parks, G.C. Campbell, A. Yezersets, N.W. Currier, L.E. Campbell, Further evidence of multiple NOx sorption sites on NOx storage/reduction catalysts, *Catal. Today* 96 (2004) 21–30, <https://doi.org/10.1016/j.cattod.2004.05.004>.
- [48] T.C. Watling, P.D. Bolton, D. Swallow, Comparison of different kinetic models for NOX storage on a lean NOX trap, *Can. J. Chem. Eng.* 92 (2014) 1506–1516, <https://doi.org/10.1002/cjce.22015>.
- [49] P.R. Dasari, R. Muncrief, M.P. Harold, Elucidating NH₃ formation during NOx reduction by CO on Pt–BaO/Al₂O₃ in excess water, *Catal. Today* 184 (2012) 43–53, <https://doi.org/10.1016/j.cattod.2011.12.009>.
- [50] R. Möller, M. Votsmeier, C. Onder, L. Guzzella, J. Gieshoff, Is oxygen storage in three-way catalysts an equilibrium controlled process? *Appl. Catal. B Environ.* 91 (2009) 30–38, <https://doi.org/10.1016/j.apcatb.2009.05.003>.
- [51] J. Gong, D. Wang, J. Li, N. Currier, A. Yezersets, Dynamic oxygen storage modeling in a three-way catalyst for natural gas engines: a dual-site and shrinking-core diffusion approach, *Appl. Catal. B Environ.* 203 (2016) 936–945, <https://doi.org/10.1016/j.apcatb.2016.11.005>.
- [52] C. Serre, F. Garin, G. Belot, G. Maire, Reactivity of Pt/Al₂O₃ and Pt–CeO₂Al₂O₃ catalysts for the oxidation of carbon monoxide by oxygen I. Catalyst characterization by TPR using CO as reducing agent, *J. Catal.* 141 (1993) 1–8, <https://doi.org/10.1006/jcat.1993.1113>.
- [53] S.E. Voltz, C.R. Morgan, D. Liederman, S.M. Jacob, Kinetic study of carbon monoxide and propylene oxidation on platinum catalysts, *Ind. Eng. Chem. Prod. Res. Dev.* 12 (1973) 294–301, <https://doi.org/10.1021/1360048a006>.
- [54] T. Bunluesin, H. Cordatos, R.J. Gorte, A study of CO oxidation kinetics on Rh/Ceria, *J. Catal.* 157 (1995) 222–226.
- [55] H. Nguyen, M.P. Harold, D. Luss, Spatiotemporal behavior of Pt/Rh/CeO₂/BaO catalyst during lean-rich cycling, *Chem. Eng. J.* 262 (2015) 464–477, <https://doi.org/10.1016/j.cej.2014.09.103>.
- [56] R.L. Muncrief, K.S. Kabin, M.P. Harold, NOx storage and reduction with propylene on Pt/BaO/alumina, *AIChE J.* 50 (2004) 2526–2540, <https://doi.org/10.1002/aic.10208>.